DISSERTATIONES
CHIMICAE
UNIVERSITATIS
TARTUENSIS
176

RASMUS PALM

Carbon materials for energy storage applications

DISSERTATIONES CHIMICAE UNIVERSITATIS TARTUENSIS
176

DISSERTATIONES CHIMICAE UNIVERSITATIS TARTUENSIS
176

RASMUS PALM

Carbon materials for energy storage applications

UNIVERSITY OF TARTU
Press

Institute of Chemistry, Faculty of Science and Technology, University of Tartu, Estonia

The dissertation is accepted for the commencement of the degree of Doctor of Philosophy in Chemistry on 5th June, 2018 by the Council of Institute of Chemistry, University of Tartu.

Supervisors: Prof. Enn Lust
University of Tartu, Estonia

PhD Heisi Kurig
University of Tartu, Estonia

Opponent: Dr Martin Månsson
KTH Royal Institute of Technology, Sweden

Commencement: August 28th, 2018, 10:15

ISSN 1406-0299
ISBN 978-9949-77-793-8 (print)
ISBN 978-9949-77-794-5 (pdf)

University of Tartu Press
www.tyk.ee

Elämä on kärsimystä
─Siiri Mari Tellervo Hyttinen

TABLE OF CONTENTS

1. LIST OF PUBLICATIONS

I. R. Palm, I. Tallo, T. Romann, H. Kurig, Methane adsorption on specially designed TiC and Mo_2C derived carbons with different pore size and surface morphology, Microporous Mesoporous Mater. 218 (2015) 167–173. doi:10.1016/j.micromeso.2015.07.016.

II. R. Palm, H. Kurig, T. Romann, U. Joost, R. Kanarbik, R. Väli, I. Tallo, T. Thomberg, A. Jänes, E. Lust, Application of Some Carbon Fabrics as Outstanding Supercapacitor Electrode Materials in Acetonitrile Based Electrolyte, J. Electrochem. Soc. 164 (2017) A453–A460. doi:10.1149/2.0831702jes.

III. R. Palm, H. Kurig, J. Aruväli, E. Lust, $NaAlH_4$/microporous carbon composite materials for reversible hydrogen storage, Microporous Mesoporous Mater. 264 (2018) 8–12. doi:10.1016/j.micromeso.2017.12.027.

Author's contribution

Paper I: Adsorption measurements and analysis of data. Mainly responsible for the preparation of the manuscript.

Paper II: Electrochemical and adsorption measurements and analysis of data. Mainly responsible for the planning of experiments. Mainly responsible for the preparation of the manuscript.

Paper III: Synthesis of composite materials, adsorption and gas amount measurements, and analysis of data. Mainly responsible for the planning of experiments. Mainly responsible for the preparation of the manuscript.

2. ABBREVIATIONS AND SYMBOLS

2D-NLDFT-HS	Two-dimensional non-linear density functional theory for heterogeneous surfaces
A	Active surface area
A_{arh}	Pre-exponent coefficient in the Arrhenius equation
AC	Alternating current
A_{el}	Geometrical area of electrode
AN	Acetonitrile
A_{Tem}	Equilibrium binding constant in the Temkin isotherm equation
b	equation constant in the Temkin isotherm
BET theory	Brunauer-Emmett-Teller theory
$BMImBF_4$	1-butyl-3-methylimidazolium tetrafluoroborate
C	Capacitance
$C'(\omega)$	Real part of complex capacitance
$C''(\omega)$	Imaginary part of complex capacitance
C_{BET}	Constant in the BET theory
CDC	Carbide-derived carbon
$C_{g,1el}$	Gravimetric capacitance per one electrode
C_p	Parallel capacitance
C_s	Series capacitance
CV	Cyclic voltammetry
d	Distance between ordered lattice plains
DC	Direct current
d_{char}	Distance between charged layers
DFT	Density functional theory
D_{phon}	Parameter related to the phonon dispersion relation
$\dot{E}$	AC potential phasor
E_{ads}	Heat of adsorption
E_{bin}	Binding energy of emitted electrons
EDL	Electric double layer
EDLC	Electrical double layer capacitor
E_{kin}	Kinetic energy of emitted electrons
E_{max}	Maximum specific energy
$E_{max,ads}$	Maximum energy of the adsorption energy distribution
$EMImBF_4$	1-ethyl-3-methylimidazolium tetrafluoroborate
$E_{min,ads}$	Minimum energy of the adsorption energy distribution
E_n	Energy
f	AC frequency
f_{chr}	Characteristic frequency
FWHM	Full width at half maximum
$FWHM_G^A(\infty)$	Raman G-peak full width at half maximum of undoped pristine graphene

$FWHM_G^A(L_a)$	Raman G-peak full width at half maximum
$h\nu$	Energy of incident photons
i	Current
$\dot{I}$	Response current phasor
I_0	Amplitude of AC
I_D	Raman D-peak intensity
i_g	Current normalized with the total mass of the electrodes
I_G	Raman G-peak intensity
IUPAC	International Union of Pure and Applied Chemistry
j	Imaginary number, $\sqrt{-1}$
K	Equilibrium coefficient
K_∞	Adsorption affinity at an infinite temperature
L_a	Correlation length
l_c	Full decay length of phonon
m_{el}	Mass of one electrode
n	Positive integer
N_A	Avogadro number
n_{ads}	Total amount of adsorbed gas
n_{ads}^{max}	Total amount of adsorbed gas at θ=1
n_{el}	Number of electrons transferred per process
n_{exc}	Amount of excess gas in the adsorption layer
n_{gas}	Amount of gas in moles
n_{het}	Characteristic parameter in the Sips isotherm equation
NLDFT	Non-local density functional theory
p	Partial pressure
P	Power
$P(\omega)$	Active power
p/p_0	Relative pressure
p_0	Saturation pressure
p_c	Critical pressure
P_{max}	Maximum specific power
PREOS	Peng-Robinson equation of state
$Q(\omega)$	Reactive power
R	Ideal gas constant
R_{el}	Resistivity
R_p	Parallel resistance
R_s	Series resistance
$S(\omega)$	Apparent power
S_{BET}	Specific surface are calculated according to the BET theory
S_{DFT}	Specific surface area calculated according to 2D-NLDFT-HS model
$S_{DFT:0.7nm}$	Specific surface area of pores with widths over 0.7 nm
S_{micro}	Specific surface area of micropores

T	Temperature
t	Time
T_c	Critical temperature
$TEMABF_4$	Triethylmethylammonium tetrafluoroborate
t_{het}	Characteristic parameter in the Toth isotherm equation
THF	Tetrahydrofuran
t_l	Average thickness of the adsorption layer
v	Scan rate of cell potential
V	Volume of gas
V_{adl}^{max}	Volume of adsorption layer at $\theta = 1$
V_{ads}	Volume of adsorbed gas
V_{DFT}	Volume of pores calculated according to 2D-NLDFT-HS model
V_m	Molar volume
V_{micro}	Volume of micropores
V_{mono}	Amount of gas adsorbed in the monolayer at maximum coverage
V_{tot}	Total volume of pores
w_{pore}	Pore width
XPS	X-ray photoelectron spectroscopy
XRD	X-ray diffraction
$Z(\omega)$	Impedance
$Z'(\omega)$	Real part of impedance
$Z''(\omega)$	Imaginary part of impedance
α_m	Projected area of the adsorbate molecule
β	Diffraction peak FWHM from which instrumentation specific effects have been subtracted
ΔE	Applied cell potential
ΔE_{rms}	Root mean square of AC potential
ΔG_{ads}	Gibbs free energy of adsorption
ΔG_{ads}^{Θ}	Gibbs free energy of adsorption at standard state
ΔH_{ads}	Enthalpy of adsorption
ΔH_{ads}^{Θ}	Enthalpy of adsorption at standard state
ΔS_{ads}	Entropy of adsorption
ΔS_{ads}^{Θ}	Entropy of adsorption at standard state
Δw	Wavenumber of Raman shift
ε_0	Dielectric constant of vacuum
ε_r	Dielectric constant of material between charged double layers
θ	Fractional surface coverage
λ	Wavelength of the incident beam
Λ	Scherrer equation shape factor
λ_0	Excitation wavelength
λ_1	Wavelength of scattered light
ξ	Acentric factor in the PREOS

ρ	Density
$\rho(r)$	Local density
τ	Average size of crystalline domains
τ_r	Characteristic relaxation time
ϕ	Phase angle
χ	Scattering angle
ω	Radial frequency

3. INTRODUCTION

The world community has almost unanimously come to an understanding that fossil fuel based economy must be converted to a renewable energy based economy to decrease the greenhouse gas emissions and to be sustainable for the future generations [1]. With renewable energy sources, it is especially necessary to provide energy accumulation systems to account for the fluctuating energy production and unsteady energy demand. At the moment being, the technology for energy storage is not developed enough to support a renewable energy based society [2–5]. Thus, the development of energy storage systems capable of supporting a renewable energy based economy is of critical importance.

Carbon materials are important for a multitude of energy storage applications as carbon properties (specific surface area, porosity, conductivity, amount of functional groups) can be controlled in a large degree by choosing the synthesis conditions and the precursor materials used for the preparation of porous carbons [6–9]. Porous carbon materials are used as electrodes in electrical double layer capacitors (EDLC), batteries and fuel cells, as adsorbents for gaseous fuel storage, as constituents of composite materials, etc. [9–12]. The properties of carbon materials influence strongly their suitability for each specific energy storage application [11–15]. It is important to establish well-optimized properties for each application to lower the cost and improve the performance of carbon materials in energy storage applications.

The relations between the specific surface area and pore volume vs. the amount of adsorbed species in various energy storage applications are of principal importance for optimized energy storage systems. The relations have been investigated, e.g. the electrode specific surface area vs. capacitance for EDLCs, the pore volume vs. the amount of adsorbed gas for energetically important gas storage applications, etc. [11–13]. In the range from low to mediocre surface areas a linear correlation is found between the amount of adsorbed species and between the specific surface area [16–19]. However, in the region of high specific surface area values, the linear relationship does not hold, i.e. the amount of adsorbed species does not depend linearly on the specific surface area calculated from the gas adsorption isotherms. Therefore, it was assumed that the influence of pore size of carbon materials in various energy storage applications has an important role [13,15,20–24]. For example, the influence of the pore size on the capacitance per specific surface area of ELDCs is still under investigation, without a resulting consensus [15,25,26]. Whereas the influence of carbon properties on performance has been investigated separately, there is a limited understanding of the complex influence of multiple properties of carbon materials on energy storage applications.

In this work, the influence of the properties of carbon materials on multiple energy storage applications is summarized and further analysis is performed. The influence of specific surface area and the pore size distribution determined

by gas adsorption methods and the average carbon material correlation length on the amount and equilibrium of energy storage is investigated primarily.

The suitability of microporous carbon fabrics as EDLC electrodes has been investigated and compared to TiC derived carbon electrodes. The influence of various carbon fabric properties, e.g. pore size and the pore size distribution, specific surface area, and electrode thickness have been determined and discussed [27].

Methane adsorption on three carbide-derived carbons with different pore size distributions and levels of graphitization has been investigated. The influence of pore size, specific surface area and the level of graphitization, i.e. disorder, on the amount of methane adsorbed has been determined and discussed [28]. Further analysis on the influence of pore size, specific surface area and the level of graphitization on the maximum amount of adsorbed methane and on the adsorption equilibrium is done.

A highly microporous carbon, most pores with widths under 2 nm, has been used as a supporting material to synthesize nanoconfined $NaAlH_4$. The influence of highly microporous supporting material on the reversible hydrogen storage applications has been investigated and discussed [29].

Based on these studies, advancement in the understanding of key carbon material properties for energy storage applications is summarized. The carbon materials properties important for optimization of efficiency and capability of different energy storage systems are ascertained.

4. LITERATURE OVERVIEW

4.1. Porous carbon materials

Porous carbons and other materials, i.e. materials with a substantial porosity and specific surface area, are used in a wide variety of applications from filtration systems, catalyst carriers, to electrode materials for various electrochemistry applications [2,3,9–11,13,14,17,18,30–33]. Porous carbons make up one of the most interesting set of materials from a wide selection of different porous materials. Carbon exists as different allotropes, e.g. diamond (sp^3 hybridisation), graphite (sp^2 hybridisation and planar bonds), fullerenes and carbon nanotubes (sp^2 hybridisation with nonplanar bonds) depending on the bonds between carbon atoms. In addition to the old classical carbon allotropes (diamond and graphite) new pure carbon structures are calculated theoretically and synthesized [33]. Carbon materials can consist of a mixture of sp^2 (graphite-like) and sp^3 (diamond-like) bonds, thus, forming an amorphous structure with a mixture of hybridised carbon bonds [8,34]. Depending on the precursor material, synthesis route, conditions of synthesis and after treatment methods the surface and bulk structure of carbon materials can be varied by a wide margin. For example, the heterogeneous microporous structure of activated carbons can produce a very large specific surface area (theoretically up to 2965 $m^2 g^{-1}$ for an infinite double-sided graphene sheet) [35]. Most carbon materials are synthesised by the pyrolysis of organic-based precursor materials, e.g. parts of vegetation, synthetic- and biopolymers, bio-oils, fossil fuels, fossil fuel products and from many more compounds [36–39].

Key parameters for porous materials are the average pore size, specific surface area and volume of pores. International Union of Pure and Applied Chemistry (IUPAC) defined pores according to the size as micropores (pores with widths under 2 nm), mesopores (pores with widths between 2 and 50 nm) and macropores (pores with widths larger than 50 nm) [40]. The surface and bulk structure of carbon materials have a strong influences on the suitability of carbon materials for different applications. For example, high surface area microporous carbon materials perform well as electrodes in EDLCs, but low surface area graphitic carbon materials as an anode electrode in Li-ion batteries [9,41]. The importance of the dominant pore shape of carbon materials in various applications and classification has been debated [42–45]. The presence of pores with variety of shapes and their influence on different applications is not completely clear because any inference on the pore shape can only be made by using neutron or synchrotron radiation based methods [43–46].

4.1.1. Carbide-derived carbons

Carbide-derived carbons (CDC) are produced from metal or non-metal (Me) containing carbides (Me_xC) by halogenation, thermal or hydrothermal pro-

cessing. The following reaction is used to produce CDCs through chlorination [33,47,48]:

$$Me_xC(s) + xy/2Cl_2(g) \rightarrow xMeCl_y(g) + C(s), \quad (1)$$

where the gaseous by-products, $xMeCl_y$, are guided through a neutralising alkaline solution by the Ar flow. The sample is cooled down in Ar flow to remove any by-products and unreacted chlorine gas. Any remaining chlorine and functional groups are reduced in hydrogen gas flow at heightened temperatures. Using higher chlorination temperatures yields CDCs with a higher level of graphitization [47–49]. CDCs can be synthesized with a narrow pore size distribution and with a lower amount of functional groups in comparison to activated carbons [47–50]. In addition to the synthesis conditions, the pore size distribution of the synthesized CDC is influenced by the crystal structure of the precursor carbide material [51,52]. The purity of CDC-s provides a higher resistance towards chemical and electrochemical reactions. It has been shown that CDCs are suitable materials for various applications, e.g. supercapacitor electrodes, adsorbents, fuel cell electrodes etc.[20,25,49,53–55].

4.1.2. Carbon fabrics

Carbon fabrics are produced by weaving carbon fibres or by carbonisation of pre-woven polymers. The polyacrylonitrile is most widely used as the precursor material amongst polymers [56,57]. Carbon fabrics have high mechanical strength, low density, and high thermal and electronic conductivity. Thus, they are used in many different applications, where aerospace and automotive industries are the largest users. In addition to previously mentioned advantages, the electrodes of EDLC made from carbon fabrics have no need for binder additives, thus, the mass of electrochemically not active material is reduced. For example, the high energy density in various electrolytes has been achieved for EDLCs with carbon fabric electrodes [58,59].

4.2. Characterisation of carbon materials

The pore and bulk structure of carbon materials vary to a large degree depending on the precursor material and synthesis conditions. Thus, carbon materials can exhibit diverse properties suitable for different applications. The following characterisation methods are used to understand better the intrinsic properties of carbon materials investigated.

Gas sorption methods are used to determine the specific surface area, volume of pores and pore size distribution of carbon materials. Commonly, the N_2 isotherms are used to derive named parameters [60,61].

Raman spectroscopy is used to compare the level of ordering between carbon materials and to determine the relative proportion of graphitic carbon in comparison to amorphous carbon. In addition, the Raman spectra are also used to calculate and compare the average correlation length of investigated carbon material [7,34,62–64].

X-ray diffraction (XRD) is used to determine the presence of crystalline substances in/on carbon materials and to calculate the average crystallite sizes of these substances [65,66].

X-ray photoelectron spectroscopy (XPS) is used to determine the chemical composition of the surface, and hence, the presence of functional groups at/in the carbon materials [67–69].

4.2.1. Gas adsorption

The physical adsorption of gases at isothermal conditions is used to characterise the volume and size distribution of open pores and the available surface of solid samples. The pressure of the analysis gas is raised stepwise during adsorption measurements and the volume of adsorbed gas is calculated after each pressure step. An adsorption isotherm, adsorbed volume, V_{ads}, vs relative pressure, $p/p_{0,}$ is completed based on the measurement data. p_0 is the saturation pressure of the adsorption gas, e.g. for N_2 p_0=0.97 bar at 77 K. The shape of the measured adsorption isotherms depends on the structure of surface. The isotherms are categorised into six types based on the shape and, thus, the porous structure of the adsorbent [61,70].

In case of physical adsorption, only van der Waals forces between the adsorbent and adsorbate contribute to the process. At equilibrium, the rates of adsorption and desorption are equal and a certain fractional surface coverage, θ, is achieved. Langmuir model describes adsorption into a monolayer and presumes the following [60,61,71,72]:

– the surface is energetically homogeneous,
– adsorption energy is constant over the surface,
– no diffusion of the adsorbed molecules,
– fixed adsorption centres,
– each adsorption centre can maintain only one molecule or atom,
– adsorbed molecules in neighbouring adsorption centres don't interact with each-other.

Langmuir isotherm is given as:

$$\theta = \frac{Kp}{(1+Kp)}, \tag{2}$$

where K is the equilibrium coefficient and $K = A_{arh} e^{\left(\frac{E_{ads}}{RT}\right)}$, E_{ads} is the heat of adsorption, A_{arh} is the pre-exponent coefficient, R is the ideal gas constant, T is the temperature and p is the partial pressure of the adsorbate.

4.2.1.1. Brunauer-Emmett-Teller theory

In 1938 Stephen Brunauer, Paul Hugh Emmett and Edward Teller formed an adsorption theory which was named after the authors as Brunauer-Emmett-Teller (BET) theory [60,61,73]. Multilayer adsorption is taken into account in the BET isotherm equation:

$$V_{ads} = \frac{V_{mono} C_{BET} p}{(p_0 - p)\left(1 + (C_{BET} - 1)\left(\frac{p}{p_0}\right)\right)}, \tag{3}$$

where V_{mono} is the amount of gas adsorbed in the monolayer at maximal coverage and C_{BET} is the BET constant.

Linearization of the BET equation yields:

$$\frac{1}{V_{ads}\left(\frac{p_0}{p} - 1\right)} = \frac{1}{V_{mono} C_{BET}} + \left(\frac{C_{BET} - 1}{V_{mono} C_{BET}}\right)\frac{p}{p_0} \tag{4}$$

When plotting $\frac{1}{V_{ads}\left(\frac{p_0}{p} - 1\right)}$ on the y-axis and $\frac{p}{p_0}$ on the x-axis the slope, s, and the intercept, i, are equivalent to the following equations:

$$s = \frac{(C_{BET} - 1)}{V_{mono} C_{BET}} \tag{5}$$

$$i = \frac{1}{V_{mono} C_{BET}} \tag{6}$$

V_{mono} can be calculated from the acquired slope and intercept:

$$V_{mono} = \frac{1}{s + i} \tag{7}$$

Thus, the specific surface area, S_{BET}, can be calculated:

$$S_{BET} = \frac{V_{mono} N_A a_m}{V_m}, \tag{8}$$

where N_A is the Avogadro number, a_m is the projected area of the adsorbate molecule and V_m is the molar volume of the adsorbate gas. BET theory for S_{BET} calculation is applicable when $\frac{p}{V_{ads}(p_0 - p)}$ vs. $\frac{p}{p_0}$ is linear and, thus, usually p/p_0 range from 0.05 to 0.2 can be used.

4.2.1.2. *t*-plot method

Adsorbents with different specific surface areas yield similarly shaped adsorption isotherms if they have similar surface characteristics and chemical composition. Thus, nonporous standard materials can be found for every material group to calculate the average adsorption layer thickness (t_l) as a function of the reduced pressure. This enables to determine the volume of micropores, the presence of mesopores and thickness of the adsorbed layer in mesopores, macropores and the external surface area by the use of *t*-plot method [60,61,74].

The amount of adsorbed gas of the investigated material is normalized to the t_l, acquired from the nonporous reference material, in the *t*-plot method. The average thickness of N_2 adsorption layer is calculated according to the equation:

$$t_l = 3.54 \left(\frac{V_{ads}}{V_{mono}} \right) \text{Å}, \tag{9}$$

where 3.54 Å is the thickness of N_2 monolayer.

V_{ads} vs t_l graph is called the *t*-plot. A nonporous material shows a straight line on the plot. The micropore volume of a porous material can be acquired by extrapolating the linear part to the V_{ads} axis.

4.2.1.3. Density functional theory

In density functional theory (DFT) the local density profile, $\rho(r)$, of a liquid is modelled on the surface or in the pores of a solid material. Theoretical adsorption isotherms characterizing porous solids are calculated from a set of modelled $\rho(r)$, i.e. kernel. The simplest DFT model is of a pore made up by two endless parallel walls, i.e. the slit-shaped pore model [75]. A weighting function is chosen for inhomogeneous confined fluids, which describes better the hard sphere direct pair correlation. The applied model is named as a non-local density functional theory (NLDFT) [76,77]. The effect of finite size, different shape

and surface roughness of pores has been investigated using various simulation methods [78–82]. The most successful DFT model thus far, in regard to corresponding to experimental adsorption isotherms, is the two-dimensional non-linear density functional theory for heterogeneous surfaces (2D-NLDFT-HS), developed by Jagiello et. al. [83]. 2D-NLDFT-HS does not presume an energetically homogeneous surface and takes into account the curvature of pores. The mentioned modifications of the DFT model deal successfully with artifacts in the pore size distributions, which were common for previous models [83,84]. Modelling experimental adsorption isotherms with a DFT model yields the pore size distribution, i.e. the distribution of volume of pores and specific surface area over a range of pore widths, w_{pore}, e.g. differential pore volume vs. w_{pore} in Figure 2.

4.2.2. Raman spectroscopy

Incident near ultraviolet, visible light or near infrared electromagnetic wave can scatter from a molecule. The scattering molecule is activated from the initial vibrational energy level to a virtual higher vibrational energy level by the scattered photon. Elastic scattering, where the molecule relaxes back to the same initial vibrational level, is called Rayleigh scattering. Molecule relaxation to a lower or higher vibrational energy level in comparison to the initial vibrational energy level is called Anti-Stokes Raman scattering or Stokes Raman scattering, correspondingly. Inelastic scattering changes the wavelength of the photon, i.e. causes a Raman shift, and is typically reported as a wavenumber, Δw [85]:

$$\Delta w = \frac{1}{\lambda_0} - \frac{1}{\lambda_1}, \tag{10}$$

where λ_0 is the excitation wavelength and λ_1 is the wavelength of the scattered light.

As the Raman scattering is caused by the chemical bonding and symmetry, which cause scattering at certain Raman shifts, it can be used to detect certain chemical compounds [86]. Carbon materials have a characteristic Raman spectrum, where the structural ordering of carbon materials influences the exact makeup of the Raman spectrum. First order Raman scattering (from 1000 to 1650 cm^{-1}) from carbon materials using near infrared or visible light for excitation is made up by two apparent wide peaks. The first peak, around 1340 cm^{-1}, is called the disorder induced (D-peak) peak. The D-peak is caused by the A_{1g} symmetry breathing mode in graphite-like structure and occurs only in the presence of defects [7,34,62–64,87–89]. The second peak, around 1580 cm^{-1}, is the so-called graphitic peak (G-peak). G-peak is caused by the in-plane bond-stretching between two carbon atoms with E_{2g} symmetry in sp^2 carbon rings and

chains [7,34,62–64,87–89]. Highly disordered single crystallite edges produce additional low-intensity D- and G-peaks, labelled D_S and G_S, respectively, at lower Raman shift wavenumbers in comparison to the D-peak and G-peak, at around 1200 cm^{-1} (D_S) and 1500 cm^{-1} (G_S) [62].

A correlation between the measured Raman spectra and between the quantitative parameters characterising the structural ordering of the carbon material has been investigated by a multitude of researchers [34,62,63,90]. The correlation between the D- and G-peak intensity, I_D and I_G, respectively, ratios and the correlation length, L_a, has been investigated. A linear correlation has been found for I_D/I_G vs. L_a or I_G/I_D vs. L_a, depending on the structural ordering of the carbon material [90]. One of the most insightful analyses and analytical solutions to the correlation was done by Ribeiro-Soares et.al. [62], where average crystallite lengths of carbons with a large variety of structural ordering were experimentally determined by tunnelling electron microscopy, scanning electron microscopy and X-ray diffraction methods. In addition, all four first-order Raman scattering peaks, described in the last paragraph, were fitted and accounted for in the analysis.

Ribeiro-Soares et. al. showed that the structural correlation length, L_a, of carbon materials, is proportional to the full width at half maximum of the G-peak ($FWHM_G^A(L_a)$) according to the following equation [62]:

$$L_a = \frac{l_C}{2} \ln\left(\frac{D_{phon}}{FWHM_G^A(L_a) - FWHM_G^A(\infty)} \right), \tag{11}$$

where D_{phon} is related to the phonon dispersion relation, D_{phon} = 95 ± 20 cm^{-1}, l_c is the full decay length of phonon, l_c = 32 ± 7 nm, and $FWHM_G^A(\infty)$ is the full width at half maximum of G-peak for undoped pristine graphene, $FWHM_G^A(\infty)$ = 15 ± 3 cm^{-1}. The l_c, C, and $FWHM_G^A(\infty)$ values have been calculated and discussed by Ribeiro-Soares et. al. [62].

4.2.4. X-ray photoelectron spectroscopy

The photoelectric effect is the emission of electrons from a material caused by a flux of incident photons. The binding energy, E_{bin}, of the emitted electron is characteristic for the host atom and of the orbital, from which the electron was emitted. During the measurement of X-ray photoelectron spectroscopy (XPS), the kinetic energies, E_{kin}, of emitted electrons are measured and electron E_{bin} is calculated [91]:

$$E_{bin} = h\nu - E_{kin}, \tag{12}$$

where $h\nu$ is the energy of the incident photons. Emitted electron counts at different E_{bin} are used to calculate the chemical composition of the investigated material with the presumption that the number of electrons recorded is proportional to the number of atoms in a given state [92]. The chemical composition can only be determined from the topmost few nanometre layers of the investigated material. Thus, proving the XPS method to be most suited for characterisation of the chemical composition of the surface [67–69].

4.2.3. X-ray diffraction

Because of the wave-like behaviour of electromagnetic waves, X-rays can interfere destructively or constructively [93,94]. Constructive interference from an ordered homogeneous system, i.e. a perfect single crystal, is described by Bragg's law [93–95]:

$$2d\sin(\chi) = n\lambda, \tag{13}$$

where d is the distance between the ordered lattice planes, χ is the scattering angle, n is a positive integer and λ is the wavelength of the incident beam.

The width of the diffraction peak is caused by instrument characteristics (e.g. non-monochromatic incident radiation, radiation source geometry, misalignments of the experimental setup) and by the sample (concentration gradients, micro-strains, defects in the crystal structure and the crystallite domain size). The diffraction peak width broadening caused by the crystalline domain size is described by the Scherrer equation [93,94,96]:

$$\tau = \frac{\Lambda\lambda}{\beta\cos(\chi)}, \tag{14}$$

where τ is the average crystalline domain size, Λ is the shape factor and β is the diffraction peak full width at half maximum (FWHM) after width broadening caused by instrumentation specific effects has been subtracted.

The upper and lower crystalline domain sizes, which can be precisely determined with the Scherrer equation, are limited by the instrumentation peak broadening and by inhomogeneous strain and crystal lattice imperfections, respectively. Crystalline domain sizes between several nanometers and a hundred nanometers can be determined with precision [97].

Whole powder pattern fitting was made possible by developments in the computational instrumentation and the development of Le Bail and Pawley pattern decompositions from the Rietveld method [94,98]. In addition to being able to refine cell parameters and determine the space group, it is possible to analyse the size-strain influence on the peak broadening with the help of formula accounting for the angular dependence of the full width at half maximum [94,99].

4.3. Applicability of carbon materials in energy storage systems

The huge variety of carbon materials, which can be synthesized from different precursor materials using various synthesis methods and conditions, necessitates a deeper understanding of the carbon materials properties influence on different applications. Properties of carbon materials, e.g. the average pore size, pore size distribution, particle size distribution, level of graphitization, electronic conductivity, density etc., influence the suitability of the carbon material for energy storage applications, where the relevant properties are determined by the application details [5,30,33,56]. Applications involving ion or molecule diffusion into the carbon material are strongly influenced by the composition of the porous structure of carbon materials, whereas, the amount of energy stored is mainly determined by the active surface area value [11–13]. The investigation of the suitability of structures and properties of various carbon materials for different energy storage applications gives a fundamental insight into physical and chemical processes and supports the development of novel and optimised energy storage materials.

4.3.1. Electrical double layer capacitors

The potential to store energy in the electrical double layer (EDL) and the use of this effect in an electrical double layer capacitor (EDLC) was already shown by H. I. Becker, from General Electric, in a patent in 1957 [100]. The electrical double layer is formed under electrical potential at the electrode/electrolyte interface. The use of high surface area electrodes is paramount to achieve high enough energy densities to be useful in energy storage applications [9,101,102]. To be usable in practical applications, the formed EDL must be stable over time, form reversibly and have a high charge density [9,101,102]. All of the components of EDLCs: electrodes, electrolytes, separators and current collectors; have been investigated to improve the overall performance and gain a better understanding of the processes involved in EDLC-s [101–104].

In an ideally capacitive EDLC no Faradic processes are present at the applicable cell potential region. At a constant cell potential scan rate a current, *i*, goes through the system. Thus, for an ideally capcitive system the absolute values of *i* during charging and discharging are equal and depend linearly on applied cell potential, i.e. *i* vs cell potential has a rectangular-like shape [13,49,105,106]. Capacitance, *C*, for an ideally capacitive system can be calculated according to Eq. 15:

$$C = \varepsilon_r \varepsilon_0 \frac{A}{d_{char}}, \tag{15}$$

where ε_r and ε_0 are the dielectric constant of the material between the charged double layers and the dielectric constant of vacuum, respectively, A is the active surface area of the electrode and d_{char} is the distance between the charged layers. Therefore, the capacitance of EDLCs should increase with the use of higher surface area electrode materials. The distance d_{char} is set by the sum of atomic radii of the electrode materials atoms and the electrolyte ions forming the electric double layer.

The energy, E_n, and power, P, of the EDLC depend on the square of the applicable cell potential, ΔE:

$$E_n = \frac{\Delta E^2 C}{2}, \tag{16}$$

$$P = \frac{\Delta E^2}{4 R_{el}}, \tag{17}$$

where R_{el} is the sum of resistivities of the electrode and electrolyte. Thus, for improved power and energy densities, a wide applicable cell potential range is of critical importance.

Electrolytes and electrolyte mixtures have been investigated for use in EDLCs [107–115]. Aqueous electrolytes, e.g. 1 M H_2SO_4, 6 M KOH or 1 M Na_2SO_4 in water solution, have high conductivity, are less sensitive to impurities and are cheaper [101,110]. The applicable cell potential for aqueous electrolytes is limited by the electrochemical stability of water. The standard potential, 1.23 V, of electrolysis of water limits applicable cell potential. Thus, the maximal power and energy density of aqueous electrolyte based EDLCs is remarkably lower [110,112]. Neutral aqueous electrolytes, e.g. 1 M Li_2SO_4, have been shown to perform well at cell potentials up to 2.2 V, alas, the Faradic side-processes can be argued to be present already at $\Delta E > 1.2$ V [112,113].

Ionic liquids offer an almost limitless number of compounds, and thus, they are possible candidates for suitable electrolytes, as there are numerous cations and anions to form a room temperature liquid salt [110,114]. Ionic liquids offer a wide applicable cell potential range, up to 5.4 V, but have low conductivity, limited applicable temperature region, high price, and ILs are sensitive towards impurities [110,115]. The small (≤ 1 M) organic solvent (acetonitrile, propylene carbonate and γ-butyrolactone) addition to ionic liquid (1-ethyl-3-methylimidazolium tetrafluoroborate, $EMImBF_4$) electrolyte has been investigated in EDLCs to decrease the viscosity, increase conductivity, decrease melting temperature and, ultimately, improve the electrochemical performance of EDLCs by R. Palm et. al. [107,108]. It was shown that the melting temperature and viscosity decrease and the conductivity increase when > 0.5 M of the organic solvent was added. Alas, the improvement in physical properties did not improve the electrochemical performance of EDLCs as the electrochemical

stability, power density and energy density decreased. Using a mixture of two ionic liquids, $EMImBF_4$ and 1-butyl-3-methylimidazolium tetrafluoroborate ($BMImBF_4$), as an EDLC electrolyte to improve the EDLC performance has been investigated by R. Palm et. al. [109]. $EMImBF_4$ has a high melting temperature, but low resistivity and a wide region of electrochemical stability. $BMImBF_4$ has a lower melting temperature but higher resistivity. At low $BMImBF_4$ concentrations, < 0.5 M, the effect on the melting temperature and on the electrochemical performance was negligible. From concentrations > 0.5 M the melting temperature decreased remarkably, but also the electrochemical performance of EDLCs with the ionic liquid mixture electrolyte degraded, as power and energy densities decreased.

Tertiary ammonium salts in acetonitrile, various carbonates or mixtures of carbonates are usually used as an organic solvent-based electrolyte. Organic solvent based electrolytes have higher conductivity, lower applicable temperature limit, but decreased applicable cell potentials, $\Delta E < 3.5$ V, in comparison to ionic liquids [110].

Depending on the used precursor materials and synthesis conditions the carbonaceous materials can be electrochemically stable over a wide cell potential region, have a large specific surface area and have high electronic conductivity. Thus, carbon materials are ideally suited for electrodes in EDLCs [9,15, 18,24,58,59]. Functionalisation of carbon materials, e.g. nitrogen or oxygen-containing functional groups, has been investigated to increase the energy density of EDLCs through pseudo-capacitive Faradic processes [116,117]. Alas, the improvement in energy density is counteracted by the decreased reversibility of the system caused by the appearance of Faradic processes. The effect of pore size and specific surface area to the capacitance value of EDLCs has been investigated to discern optimal structures for electrode materials [13,15,18, 24,25]. An anomalous increase in capacitance normalized by electrode surface area in case of sub-nanometre pores was shown by Chimola et.al. [25] and the effect was explained by the decrease in the size of solvate shell around the adsorbed ions in smaller pores discussed as well by Aurbach et. al and by Lust et.al [118–120].

4.3.1.1. Cyclic voltammetry

During cyclic voltammetry (CV) measurements the potential of the electrochemical system is increased and then decreased at a constant scan rate, v, given in units of mV s^{-1}, and the current, i, is measured. In the case of a symmetrical two electrode cell the potential between the identical electrodes is measured, i.e. the cell potential, ΔE, and the polarisation of the electrodes is not individually determined. The CV measurement is conducted between two cell potentials, where the system starts and ends the final measurement at the same cell potential. In case of a Faradic process, the CV measurement will exhibit a current peak during the increase of the cell potential. If the Faradic process is

totally reversible, and n_{el} electrons are transferred per process, a current peak will be present during the decrease of the cell potential with a potential shift of $59/n_{el}$ mV in comparison to the current peak from the increase of the cell potential. If the potential shift is larger than $59/n_{el}$ mV, then the Faradic process is reversible only partially. In the case of irreversible processes, there is no current peak during the decrease of the cell potential. In an ideally capacitive system, there are no current peaks during the increase and the decrease of the cell potential [13,49,105,106,121].

Thus, the gravimetric capacitance per one electrode in case of symmetric ideally capacitive system can be calculated from CV data according to Eq. 18:

$$C_{g,1el}(t) = \frac{2i}{v(t)m_{el}}, \tag{18}$$

where t is time and m_{el} is the mass of one electrode. For ideally polarisable EDLC system the $C_{g,1el}(t)$ is independent of potential scan rate applied.

4.3.1.2. Electrochemical impedance spectroscopy

In case of electrochemical impedance spectroscopy (EIS) alternating current (AC) is applied in addition to a constant cell potential attained with direct current (DC). The amplitude of the AC has to be low enough (from ±5 to ±10 mV) so that the current-overpotential relation would be linear, i.e. the current caused by the excitation would have exactly the same frequency and no higher harmonics would be produced. The system is measured over a range of AC frequencies, f. Processes of different timescales are measured depending on the applied frequency of AC [121,122].

The response current phasor, $\dot{I}$, with an amplitude of I_0 is shifted by a phase angle, ϕ, in comparison to the applied sinusoidal AC potential, if there are additional capacitive or inductive effects:

$$\dot{I} = I_0 \sin(\omega t + \phi), \tag{19}$$

where ω is the radial frequency and $\omega = 2\pi f$. For simple resistive circuits $\phi = 0$.

Impedance, i.e. complex resistance, consists of the real, $Z'(\omega)$, and imaginary, $Z''(\omega)$, parts [121–123]. Impedance is calculated from the $\dot{I}$ and applied AC potentials phasors, $\dot{E}$, according to the Ohm's law:

$$Z(\omega) = \frac{\dot{E}}{\dot{I}} = Z'(\omega) - jZ''(\omega), \tag{20}$$

where j = $\sqrt{-1}$.

The ratio of $Z'(\omega)$ and $Z''(\omega)$ can be calculated from the measured phase angle:

$$\tan\phi = \frac{Z''(\omega)}{Z'(\omega)} \tag{21}$$

A Nyquist plot, Z'' (ω) vs $Z'(\omega)$, gives information about the processes occurring in the system at different frequencies. EDLCs have a characteristic Nyquist plot shape: EDLCs form a semicircle corresponding to the resistive-capacitive behaviour of electrodes at high frequencies [121–123], in the range of medium frequencies a 45° inclination emerges, and a vertical is observed at the lowest frequencies. The vertical line towards Z'' (ω) values corresponds the so-called ideal capacitive behaviour of EDLCs ($f \to 0$) and the 45° inclination corresponds to the diffusion of ions inside the pores [122,123].

If the system is modelled with the combination of a capacitive and resistive elements in an equivalent circuit, it can be described by the following parameters: Series resistance, R_s, series capacitance, C_s, parallel resistance, R_p, and parallel capacitance, C_p, which are given by to the following expressions [122–124]:

$$R_s = Z'(\omega), \tag{22}$$

$$C_s = -\frac{1}{\omega Z''(\omega)}, \tag{23}$$

$$R_p = R_s\left(1 + \frac{1}{\tan^2\left(\frac{Z'(\omega)}{Z''(\omega)}\right)}\right), \tag{24}$$

$$C_p = C_s\left(1 + \tan^2\left(\frac{Z'(\omega)}{Z''(\omega)}\right)\right) \tag{25}$$

For EDLCs the R_s at Z''=0 (intercept at the high-frequency edge of the semicircle) corresponds to the system resistance. The second intercept at Z''=0 of the semicircle at lower frequencies corresponds to the pore resistance. The R_s, corresponding to the system resistance, and C_s value, corresponding to purely capacitive behaviour (at low enough frequencies, f < 0.01 Hz), are used to calculate the maximal specific energy, E_{max}, and maximal specific power, P_{max}, of symmetric two-electrode EDLC system [49]:

$$E_{\max} = \frac{\Delta E^2 C_s A_{el}}{2m_{el}}, \tag{26}$$

$$P_{\max} = \frac{\Delta E^2 A_{el}}{4R_s m_{el}}, \tag{27}$$

where A_{el} is the geometric area of one electrode.

C_s can be defined as a complex function, $C_s(\omega)=C'(\omega)-jC''(\omega)$, where $C'(\omega)$ is the real part and $C''(\omega)$ is the imaginary part of capacitance. $C'(\omega)$ and $C''(\omega)$ are expressed as follows:

$$C'(\omega) = -\frac{Z''(\omega)}{\omega|Z(\omega)|^2}, \tag{28}$$

$$C''(\omega) = \frac{Z'(\omega)}{\omega|Z(\omega)|^2} \tag{29}$$

Apparent power, $S(\omega)$, determined by EIS is a complex function, $S(\omega)= P(\omega)+jQ(\omega)$, where $P(\omega)$ is the active power and $Q(\omega)$ is the reactive power. $P(\omega)$ and $Q(\omega)$ are expressed through imaginary and real part of capacitance as follows [123,124]:

$$P(\omega) = \omega C''(\omega)|\Delta E_{rms}|^2, \tag{30}$$

$$Q(\omega) = -\omega C'(\omega)|\Delta E_{rms}|^2, \tag{31}$$

where ΔE_{rms} is the root mean square of the AC potential and for a sinusoidal wave $\Delta E_{rms} = \Delta E_{\max} / \sqrt{2}$, where $\Delta E_{\max}$ is the maximum amplitude of the AC potential.

At the characteristic frequency, f_{chr}, the normalized active power ($|P(\omega)|/|S(\omega)|$) and normalized reactive power ($|Q(\omega)|/|S(\omega)|$) are equal, i.e. the frequency at which half of the energy stored is released. The characteristic relaxation time, τ_r, the time which is required to release half of the stored energy, is calculated from the f_{chr}:

$$\tau_r = \frac{1}{2\pi f_{chr}} \tag{32}$$

4.3.1. Methane adsorption

Natural gas is used as a transitional fuel before the full implementation of a renewable energy based society. CO_2 emissions from combustion of natural gas are lower per energy unit than from any other fossil fuel, except biogas [125]. The main component of natural gas is methane, thus, methane is a good sample gas to investigate the adsorption of natural gas for energy storage applications. Methane adsorption on various adsorbents, from carbonaceous to zeolites and metal-organic frameworks, has been studied for methane storage and gas sequestration applications [11,17,22,53,125–129]. Carbonaceous materials can be synthesized with a wide variety of properties and with high purity, i.e. almost no functional groups at carbon surfaces. Thus, they are of special interest in investigating the influence of surface morphology, i.e. pore size, specific surface area and graphitization, on the methane adsorption.

A linear correlation between the amount of adsorbed methane and the specific surface area or the micropore volume of adsorbents has been shown for a multitude of carbon materials [11,17]. Nevertheless, the amount of methane adsorbed per specific surface area at 25 °C and 3.5 MPa varied from 0.004 to 0.0067 mmol m^{-2} for two carbon materials with almost identical specific surface areas nearly 1115 m^2 g^{-1} [53,125]. Pores under 0.7 nm have been shown to adsorb methane at lower partial pressures and pores under 1 nm have been shown to adsorb more methane per specific surface area in comparison to larger pores [22,23]. Although methane adsorption has been investigated on carbon materials with different levels of graphitization, the influence of the structural ordering of carbon materials on the amount of methane adsorbed is not well established [11,17,22,23,53,125,129].

4.3.1.1. Equation of state

Ideal gas law, $pV=n_{gas}RT$, where p is pressure, V is volume, n_{gas} is amount of gas in moles, R is the universal gas constant and T is temperature, is an equation of state for gases which makes the presumption that gas molecules are mathematical points in space and there are no interactions between the gas molecules. The ideal gas law is strictly applicable only at low pressures, high temperatures and for monoatomic gases. As real gases are not mathematical points in space but have a molecular volume, might have an asymmetric shape, and interact with each other through the van der Waals forces, various equations of state have been proposed for gases [130–133].

Peng and Robinson proposed a new equation of state (PREOS) in 1976 [130] as a development to van der Waals [131], Redlich and Kwong [132] and Soave [133] equations of state. PREOS takes into account the asymmetry of investigated substances, the critical parameters of the substances and the molecular volume of the substances:

$$p = \frac{RT}{V_m - b} - \frac{\alpha a}{V_m^2 + 2bV_m - b^2}, \tag{33}$$

$$a = \frac{0.4572\, R^2 T_c^2}{p_c}, \tag{34}$$

$$b = \frac{0.07780\, RT_c}{p_c}, \tag{35}$$

$$\alpha = \left(1 + \kappa\left(1 - \left(\frac{T}{T_c}\right)^{0,5}\right)\right)^2, \tag{36}$$

$$\kappa = 0,37464 + 1,54226\xi - 0,26992\xi^2, \tag{37}$$

where ξ is the acentric factor, T_c is the critical temperature, p_c is the critical pressure and V_m is the molar volume. Parameter a is related to the inter-molecular attraction forces and b is related to the size of the molecule. PREOS is accurate at the critical point, especially for the calculations of compressibility and liquid density [130].

4.3.1.2. Adsorption isotherms

The excess gas, n_{exc}, amount in the adsorption layer in comparison to the gas phase is determined during measurements. At high pressures the gas phase density, ρ, is large enough to cause a deviation between the measured n_{exc} and the total amount of adsorbed gas, n_{ads} [129,134]:

$$n_{exc} = \theta(n_{ads}^{max} - V_{adl}^{max}\rho) \tag{38}$$

$$n_{ads} = \theta n_{ads}^{max} \tag{39}$$

where θ is the fractional surface coverage, n_{ads}^{max} is the amount of adsorbed gas at $\theta = 1$ and V_{adl}^{max} is the volume of the adsorption layer at $\theta = 1$.

To establish θ and n_{ads} values, it is necessary to model the measured n_{exc} isotherm with a theoretical adsorption isotherm. The Langmuir isotherm (Eq. 2) was described in the Section 4.2.1. Further isotherm equations have been

developed to characterise a system that does not meet the presumptions of the Langmuir isotherm [60,71,72,135–137].

Sips isotherm equation (Langmuir-Freundlich) presumes a Gaussian distribution of adsorption energies, where the Sips isotherm equation is an averaged Langmuir isotherm over the energy distribution [135]. Thus, Sips isotherm equation has a similar form to Langmuir equation:

$$n_{ads} = n_{ads}^{\max} \frac{(Kp)^{1/n_{het}}}{1+(Kp)^{1/n_{het}}}, \tag{40}$$

where K is the equilibrium coefficient and n_{het} is characteristic parameter taking into account the systems heterogeneity of system. If n_{het} is unity, the Sips equation yields the Langmuir equation for a homogeneous surface.

It is known that the Toth equation is an empirical adsorption isotherm equation, which describes well many systems, where $\theta < 1$ [136]:

$$n_{ads} = n_{ads}^{\max} \frac{Kp}{\left[1+(Kp)^{t}\right]^{1/t_{het}}}, \tag{41}$$

where t_{het} is a parameter characterising the system heterogeneity and, similarly to the parameter n_{het} in Sips equation (Eq, 40), when t_{het} is unity the Toth equation is identical to the Langmuir equation.

Presuming a patchwise surface topography, Langmuir isotherm is applicable for each patch and a uniform energy distribution the Unilan equation is obtained [60]:

$$n_{ads} = \frac{n_{ads}^{\max}}{2s} \ln\left(\frac{1+\bar{K}e^{s}p}{1+\bar{K}e^{-s}p}\right), \tag{42}$$

where

$$\bar{K} = K_{\infty} \exp\left(\frac{\bar{E}}{RT}\right), \tag{43}$$

$$\bar{E} = \frac{E_{\max,ads} + E_{\min,ads}}{2}, \tag{44}$$

$$s = \frac{E_{\max,ads} - E_{\min,ads}}{2RT}, \tag{45}$$

$E_{max,ads}$ and $E_{min,ads}$ are the maximum and minimum energies of the distribution, K_∞ is the adsorption affinity at an infinite temperature and s is a parameter characterising the systems heterogeneity of system. If $s = 0$ the Unilan equation [60] is reduced into a Langmuir equation.

The Temkin isotherm presumes that the heat of adsorption decreases linearly with the increase in surface coverage [137]:

$$n_{ads} = B \ln A_{Tem} + B \ln p\,, \tag{46}$$

where A_{Tem} is the equilibrium binding constant, B is related to the heat of adsorption and $B=RT/b$, where b is the Temkin isotherm constant.

4.3.1.3. Thermodynamics of adsorption

The thermodynamics of an adsorption process at equilibrium is described through the change of enthalpy (ΔH_{ads}), entropy (ΔS_{ads}) and Gibbs free energy (ΔG_{ads}):

$$\Delta G_{ads} = \Delta H_{ads} - T\Delta S_{ads} \tag{47}$$

Combining Gibbs free energy equation (Eq. 47) with Gibbs isotherm equation (Eq. 48) the linear form of the van't Hoff equation is given as (Eq. 49) [61,138]:

$$\Delta G^{\Theta}_{ads} = -RT \ln K\,, \tag{48}$$

$$\ln K = -\frac{\Delta H^{\Theta}_{ads}}{RT} + \frac{\Delta S^{\Theta}_{ads}}{R}\,, \tag{49}$$

where K is the adsorption-desorption equilibrium constant, R is the ideal gas constant, T is the temperature and ΔG^{Θ}_{ads}, ΔH^{Θ}_{ads} and ΔS^{Θ}_{ads} are the changes of Gibbs free energy, enthalpy and entropy at standard state (0.1 MPa), respectively. Plotting ln(K) vs. 1/T, the slope is equal to $-\Delta H^{\Theta}_{ads}/R$ and the intercept is equal to $\Delta S^{\Theta}_{ads}/R$.

4.3.2. Hydrogen storage

Hydrogen has a low density (0.09 g L^{-1} at 0 °C and 0.1 MPa) and, therefore, different methods have been used to increase the density of hydrogen to improve the energy density of hydrogen storage systems. Compressing hydro-

gen increases the density of hydrogen (41 g L^{-1} at 0 °C and 70 MPa), but is energy demanding. The energy required to compress hydrogen to 70 MPa is more than 10% of the energy stored in the compressed hydrogen. The high diffusivity (0.61 cm^2 s^{-1} in air at 0.1 MPa and 273.15 K), low minimum ignition energy (20 μJ), and wide concentration range for combustion (from 4 to 75 vol% in air) and explosion (from 18 to 59 vol% in air) of hydrogen increase the hydrogen storage hazards, especially at high pressures. By compressing hydrogen up to high pressures the risk of hydrogen embrittlement is increased and, thus, the price of the storage medium is also increased. Cooling hydrogen to the liquid state at 20 K increases the hydrogen density to 70 g L^{-1}, but more than 20% of the stored energy is consumed during the liquefaction process. In addition, storage of liquid hydrogen demands continuous cooling or the release of H_2 overpressure that accumulates during warming over longer times of storage. High requirements in regards to insulation, pressure control, heating etc. increase the mass and the price of the liquid hydrogen storage systems [5,139].

Physical adsorption of hydrogen in porous materials, for example, into carbon, into silicates and zeolites, is nearly reversible and efficient due to the weak Van der Waals interactions between hydrogen and the adsorbent [16,140]. One of the highest amounts of adsorbed hydrogen, 3.75 wt% of hydrogen, at the temperature of liquid nitrogen, 77 K, and at 0.1 MPa has been achieved with micro carbon spheres produced from mesophase pitches as an adsorbent [141]. Thus, for hydrogen storage through physical adsorption increased pressures and lowered temperatures are necessary. In addition, carbon-based adsorbent materials have a low density and, thus, the achieved hydrogen densities per volume are also relatively low.

4.3.2.1. Hydrides

Compounds including a metal (A) or two metals (A and B) bonded with hydrogen (H) are called metal hydrides (AH_y and AB_xH_y, respectively). In the hydride compounds hydrogen has either an ionic or covalent bond to the metal atoms, depending on the electronic properties of the hydride forming metal [139,142]. Interstitial hydrides absorb hydrogen reversibly inside the crystal lattice vacancies. For interstitial hydrides, A in AH_y or in AB_xH_y is a transition metal (Pd, Ti, V e.g.), rare earth metal (La, Pr, Gd or Sm) or Mg. In the case of interstitial hydrides, hydrogen molecules dissociate into the atomic form on the metal surface layer before diffusing into the crystal structure of the bulk metal. T. Graham was the first to report the accumulation of hydrogen inside a metal, Pd, [143], where 0.6 wt% of H_2 was absorbed at 0.3 MPa forming the interstitial hydride $PdH_{0.6}$. Thus far many other metal hydrides have been investigated for hydrogen storage applications. However, the main obstacles for practical exploitation of transition or rare earth metal hydrides are low hydrogen content and the high price of materials used [139,142]. One of the most promising metal

hydrides is MgH_2, where hydrogen is mostly ionically bonded. MgH_2 has a high hydrogen content (7.6 wt%) and relatively low cost, but the temperature of hydrogen release for the material is too high (> 300 °C at 0.1 MPa) and the hydrogen absorption kinetics is too slow for practical applications [5,139,142].

Hydrides with the chemical formula $A_xMe_yH_z$, where A is an element from the first or second group of the periodic table and Me is either boron or aluminium, are called complex hydrides [139,142]. Due to their high hydrogen content, low density and abundant constituents, the most promising complex hydrides for hydrogen storage are $NaAlH_4$ and $LiAlH_4$ [5,139,142]. $LiAlH_4$ has a very high hydrogen content (10.5 wt%), but the hydrogenation of Li_3AlH_6 back into $LiAlH_4$ is not possible under reasonable physical conditions (over 10 MPa of hydrogen partial pressure at 25 °C even with the addition of organic solvent tetrahydrofuran).In addition, the supply of Li is limited and the price is rising, especially because of the growing battery industry [139,142,144,145]. In comparison, the complex hydride $NaAlH_4$ is made up of chemical elements which are more abundant in the earth's crust. The capability to release hydrogen reversibly has been shown, although the hydrogen content is lower (7.4 wt%). In addition to the previous points, the relatively low pressure and temperature necessary for reloading with hydrogen make $NaAlH_4$ one of the best solid-state materials for large-scale hydrogen storage [5,139,142,144].

4.3.2.2. $NaAlH_4$ for hydrogen storage

The thermal decomposition of $NaAlH_4$ occurs through three consecutive reactions [139,142,146]:

$$NaAlH_4 \rightarrow 1/3\ Na_3AlH_6 + 2/3\ Al + H_2 \quad (50)$$

$$1/3\ Na_3AlH_6 \rightarrow NaH + 1/3\ Al + ½\ H_2 \quad (51)$$

$$NaH \rightarrow Na + ½\ H_2 \quad (52)$$

Only the first two reactions, starting at 150 °C and around 250 °C, respectively, are reversible and release 5.4 wt% of hydrogen [147]. In practice, the first decomposition reaction in bulk $NaAlH_4$ is kinetically limited and, thus, most of the hydrogen from the first decomposition reaction is released at temperatures higher than 180 °C, after the melting of $NaAlH_4$.

The temperature and kinetics of hydrogen release from $NaAlH_4$ can be improved by decreasing the particle size, e.g. by ball-milling of $NaAlH_4$ powder. $NaAlH_4$ ball milled for 2 h released 2.9 wt% of hydrogen in 120 min already at 160 °C [148]. Hydrogenation of ball-milled $NaAlH_4$ is shown at lower temperatures and pressures than for bulk $NaAlH_4$, where 4 wt% of hydrogen was absorbed during 180 min at 150 °C and at a hydrogen pressure of 8.8 MPa [148]. However, already after a few hydrogenation/dehydrogenation cycles the

ball-milled $NaAlH_4$ aggregates back into the bulk material. This is promoted by the increased diffusion of $NaAlH_4$ at higher temperatures necessary for release of hydrogen. The addition of catalysts decreases the hydrogen release temperature of $NaAlH_4$. For example, the ball-milling of 0.5 mol-% of $TiCl_3$ into $NaAlH_4$ increased the amount of released hydrogen at 160 °C to 5 wt%. Formation of the more stable $TiAl_3$ alloy caused higher mol-%, > 0.5 mol-%, of $TiCl_3$ to increase the hydrogenation and dehydrogenation pressure [149]. The kinetics of hydrogen release has been enhanced by the addition of $TiCl_3$, where 0.9 mol-% of $TiCl_3$ addition into $NaAlH_4$ induced the release of 3 wt% of hydrogen already at 125 °C in 4 hours [150].

Deposition of $NaAlH_4$ inside the pores of a supporting material as nanoparticles, i.e. nanoconfinement of $NaAlH_4$, improves the hydrogen release temperature, kinetics, and reversibility of hydrogen release [139,142]. The supporting material must have a large specific surface area, high thermal and chemical stability, and porosity suitable for confining the complex metal hydride. Carbon-based supporting materials are well-suited for this purpose due to the large variability and control over the properties (pore size, specific surface area, functional groups etc.) of carbon materials through the synthesis and after-treatment conditions [33,47–49]. Baldé et. al. [151] showed that nanoconfined small $NaAlH_4$ particles, 2–10 nm, inside of the carbon nanofibers started releasing hydrogen already at 70 °C and the hydrogenation process of decomposed particles back to $NaAlH_4$ was possible at 115 °C at a hydrogen pressure of 2 MPa. The temperature of hydrogen release increases with the increased size of $NaAlH_4$ particles and hydrogen release at 70 °C was achieved for a composite material containing only 2 wt% of $NaAlH_4$ [151]. The influence of the deposited wt% of $NaAlH_4$ inside the $NaAlH_4$/carbon composite material has been studied by Gao et. al [152]. Between 5 wt% and 80 wt% of $NaAlH_4$ was deposited inside a nanoporous carbon material and the composites with $NaAlH_4$ content from 5 wt% to 30 wt% started releasing hydrogen already at 150 °C [152]. The addition of 3 wt% of $TiCl_3$ as a catalyst into nanoconfined $NaAlH_4$ (33.3 wt%) decreased the maximum temperature of hydrogen release peak maximum temperature from 176 °C to 125 °C, at a temperature ramp rate of 5 °C min^{-1}. However, the amount of hydrogen absorbed during hydrogenation of the decomposed particles is decreases already after the application of four dehydrogenation/hydrogenation cycles [153].

5. AIM OF THE STUDY

The aim of this work was to determine the influence of carbon material surface properties on the performance of these carbon materials in energy storage applications. The influence of specific surface area, pore size and its distribution and structural ordering of carbon materials on the amount of energy stored and on the kinetics of energy storage was to be determined. The following research was performed to achieve that aim:

The influence of the specific surface area and porosity on the adsorption of charged species was investigated through the use of different carbon materials as electrode materials in electric double layer capacitors.

The influence of specific surface area, porosity and structural ordering on the adsorption of neutrally charged species was investigated through the use of different carbide-derived carbons for the adsorption of methane.

The influence of a highly microporous and high surface area carbon material on the confinement of a complex metal hydride for hydrogen storage was investigated.

6. EXPERIMENTAL

6.1. Preparation of CDC materials

Titanium carbide (TiC with purity 99.5 %, -325 mesh powder, Sigma-Aldrich) or molybdenum carbide (Mo_2C with purity 99.5 %, -325 mesh powder, Sigma-Aldrich) was etched with Cl_2 or HCl (AGA from The Linde Group, 99,99 %) in a stationary quartz bed reactor at fixed reaction temperatures: 950 or 1100 °C for TiC-CDC 950 °C and TiC-CDC 1100 °C HCl, and 1000 °C for Mo_2C-CDC 1000 °C, respectively. A gas flow rate of 50 ml min^{-1} or 100 ml min^{-1} was applied for Cl_2 or HCl, respectively. Chlorination by-products were removed with Ar flow. The residual chlorine and oxygen-containing functional groups were removed during 1.5 h of applied H_2 flow at 800 °C [47,49].

6.2. Synthesis of scaffold supported $NaAlH_4$ composite materials

The synthesis and storage of $NaAlH_4$/carbon composites were performed in closed Ar atmosphere. A solution of 0.05 g ml^{-1} sodium aluminium hydride ($NaAlH_4$, 90%, Sigma Aldrich) in tetrahydrofuran (THF, anhydrous, ≥ 99.9 %, Sigma-Aldrich) was prepared for the synthesis. Any insoluble impurities were removed by filtrating the solution through a glass microfiber filter (GF/B, Whatman). Cleaned and dry microporous carbon, RP-20 (Kuraray, Japan), was used as the supporting material. At each step, 2 ml of the filtrated dolution of $NaAlH_4$ in THF was added per 1 g of carbon to the dry RP-20 until the desired wt% of $NaAlH_4$ was achieved. Each time the solution of $NaAlH_4$ in THF was added, the mixture was stirred at 0 °C under 0.1 MPa of Ar for 15 minutes in order to infiltrate the solution inside the pores of RP-20. The reaction flask was stirred for 45 min under 100 Pa of Ar pressure at 23 °C to remove most of the solvent, THF. The $NaAlH_4$/RP-20 composite material was finally dried from residual solvent during 36 hours at 30 °C and 3.3 Pa of Ar. The deposited complex hydride was reformed for 10 h at 140 °C and at 18 MPa of hydrogen pressure to regenerate any decomposed $NaAlH_4$. $NaAlH_4$/RP-20 composite materials with the content of $NaAlH_4$ from 10 to 60 wt% were synthesised. Henceforward, the synthesized materials are designated as *x*$NaAlH_4$/RP-20, where *x* stands for the wt% of $NaAlH_4$ in the composite material. For the pure $NaAlH_4$ the same synthesis route was followed but without the RP-20. This was nessecary to produce a reliable comparison between confined and bulk $NaAlH_4$ capability to store hydrogen reversibly.

6.3. Surface characterisation via N_2 and CO_2 adsorption technique

Gas sorption system ASAP 2020 (Micromeritics, USA) was used to measure the adsorption and desorption isotherms of N_2 and CO_2 at 77 K and 273 K, respectively. The specific surface area (S_{BET}), the surface area of micropores (S_{micro}), the volume of micropores (V_{micro}), and the total volume of pores (V_{tot}) of carbon materials were calculated from the adsorption isotherms of N_2 (Table 1). The Brunauer-Emmett-Teller (BET) method was used to calculate the S_{BET} values [73], the *t*-plot method was used to calculate S_{micro} and V_{micro} values [74], and the amount of adsorbed gas near the saturation pressure of nitrogen (p/p_0 = 0.95) was used to calculate V_{tot}.

Table 1. Characteristic properties of studied carbon materials and carbon electrodes, calculated from the N_2 adsorption isotherm.

Carbon material	S_{BET} $m^2 g^{-1}$	S_{micro} $m^2 g^{-1}$	S_{micro}/S_{BET}	V_{tot} $cm^3 g^{-1}$	V_{micro} $cm^3 g^{-1}$	V_{micro}/V_{tot}
L-0.3-135	540	536	0.99	0.26	0.25	0.96
T-040	1240	1210	0.98	0.63	0.58	0.92
T-1-040	1130	1090	0.97	0.59	0.53	0.90
TiC-CDC 950 °C electrode	1450	1440	0.99	0.70	0.63	0.91
TiC-CDC 950 °C	1560	1550	0.99	0.75	0.68	0.91
TiC-CDC 1100 °C HCl	870	770	0.88	0.93	0.70	0.75
Mo_2C-CDC 1000 °C	820	250	0.30	1.47	0.09	0.06
RP-20	1840	1830	0.99	0.82	0.80	0.97

S_{BET} – BET specific surface area, S_{micro} – micropore area, calculated using the *t*-plot method, V_{tot} – total pore volume, V_{micro} – micropore volume

Two-dimensional non-local density functional theory model for carbons with heterogeneous surfaces (2D-NLDFT-HS) [[83,84]] was used to calculate the pore size distribution data. 2D-NLDFT-HS model was simultaneously applied to CO_2 and N_2 adsorption isotherm data [84] using SAIEUS software (v2.02, Micromeritics, USA) [154] to acquire a correct pore size distribution. The specific surface area, S_{DFT}, and pore volume, V_{DFT}, calculated with the 2D-NLDFT-HS model are presented in Table 2.

Table 2. Properties of the studied carbon materials calculated from the simultaneously fitted N_2 and CO_2 adsorption isotherms and the measured thickness of carbon-based electrode materials.

Carbon material	S_{DFT} $m^2 g^{-1}$	V_{DFT} $cm^3 g^{-1}$	$S_{DFT0.7nm}$ $m^2 g^{-1}$	Thickness mm
L-0.3-135	840	0.25	100	0.42 ± 0.02
T-040	1420	0.59	610	0.38 ± 0.02
T-1-040	1360	0.56	510	0.25 ± 0.02
TiC-CDC 950 °C electrode	1440	0.63	740	0.13 ± 0.01
TiC-CDC 950 °C	1540	0.68		
TiC-CDC 1100 °C HCl	680	0.86		
Mo_2C-CDC 1000 °C	720	1.36		
RP-20	1650	0.74		

S_{DFT} – Specific surface area calculated by applying 2D-NLDFT-HS model to the cumulative CO_2 and N_2 isotherms, V_{DFT} – Total volume of pores calculated by applying 2D-NLDFT-HS model to the cumulative CO_2 and N_2 isotherms, $S_{DFT0.7nm}$ – Specific surface area of pores with widths over 0.7 nm calculated by subtraction of specific surface area from pores with widths under 0.7 nm from S_{DFT}.

6.4. Raman spectroscopy

Raman spectra were measured using an inVia micro-Raman spectrometer (Renishaw, UK) within a wavenumber region from 50 cm^{-1} to 4000 cm^{-1} and with an excitation wavelength λ_0 = 514 nm. The first-order Raman scattering region (from 1000 to 1800 cm^{-1}) was fitted with two Lorentzian, for D- and G-peak, and two Gaussian, for G_S- and D_S-peak, functions (Figure 1) as specified by Ribeiro-Soares et. al. [62]. All the carbon materials under study were refitted with the method suggested by Ribeiro-Soares to have consistently comparable results from Raman spectroscopy. Thus, the calculated average correlation lengths, L_a, absolute values (Table 3) may somewhat differ from the ones presented in our previous articles, but the sequences between different carbon materials remain the same.

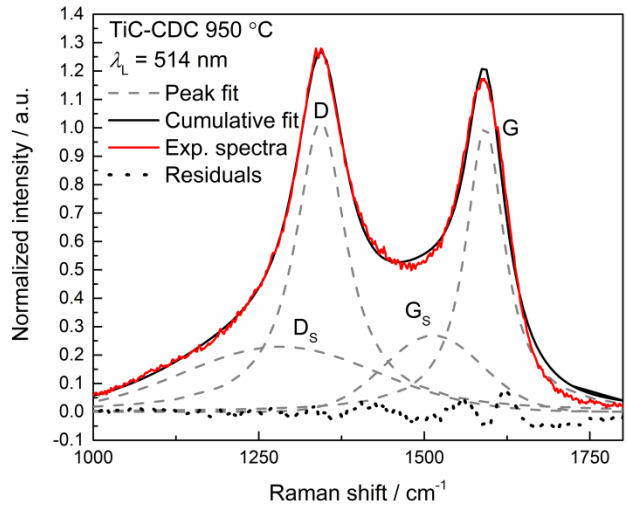

Figure 1. Raman spectra of TiC-CDC 950 °C normalized to the height of G-peak and the fit of the modelled spectra with the fit residuals, according to model by Ribeiro-Soares et. al. [62].

Table 3. Results obtained by fitting the measured Raman spectra with model according to Ribeiro-Soares et. al. [62].

Carbon material	$FWHM_G$ cm^{-1}	L_a nm	I_D/I_G
L-0.3-135	53.5	14.4	2.15
T-040	46.3	17.8	2.06
T-1-040	44.9	18.5	2.15
TiC-CDC 950 °C	71.8	8.2	1.43
TiC-CDC 1100 °C HCl	66.3	9.9	1.21
Mo_2C-CDC 1000 °C	64.0	10.6	0.69
RP-20	49.8	16.1	2.13

$FWHM_G$ – G-peak full width at half maximum, L_a –average correlation length of carbon structure calculated from G-peak FWHM [62], I_D/I_G – the ratio of integrated peak intensities, where the integrated intensities of G_S- and D_S-peak are added to the integrated intensities of G-peak and D-peak, respectively.

6.5. X-ray photoelectron spectroscopy

The chemical state and elemental composition of carbon fabrics were investigated with X-ray photoelectron spectroscopy (XPS). XPS measurements were conducted using a surface station equipped with an electron energy analyser (SCIENTA SES 100) and a non-monochromatic twin anode X-ray tube (Thermo XR3E2). The characteristic energies of the X-ray tubes were 1253.6 eV

(Mg $K\alpha_{1,2}$ FWHM 0.68 eV) and 1486.6 eV (Al $K\alpha_{1,2}$ FWHM 0.83 eV). Ultra-high vacuum conditions were applied for measurements. Average Matrix Relative Sensitivity Factors procedure [155] and the transmission function of the instrument were used to estimate the overall atomic concentrations of different compounds and elements. Casa XPS software (v2.3.12, Casa Software Ltd, UK) was used for the raw data processing. Data processing involved removal of Kα and Kβ satellites, removal of background and fitting of the XPS components. Shirley type background was used for background removal. The fitting was performed using a Gauss-Lorentz hybrid function (GL 70, Gauss 30%, Lorentz 70%). The calculated atomic percentages established are presented in Table 4.

Table 4. Atomic ratios of elements obtained using XPS method for investigated carbon fabric electrodes

Electrode material	C atom%	O atom%	Si atom%
L-0.3-135	89	8	3
T-1-040	97	3	0
T-040	96	4	0

6.6. X-ray diffraction

D8 Advance diffractometer (Bruker, Germany) with Cu Kα radiation was used for X-ray diffraction (XRD) measurements. Diffractograms were acquired at 2θ from 5° up to 90° with a total step time of 166 s and a step size of 0.0128° using a LynxEye detector. An X-ray transparent cap was used to insulate the powder sample in Ar atmosphere to hinder oxidation of the sample before and during the measurements. Full profile analysis software Topas 4.1 (Bruker, Germany) was used to calculate the crystallite sizes from the diffractograms measured.

6.7. CH_4 adsorption

Methane excess adsorption isotherms from -100 to 40 °C and methane partial pressures from 0.03 to 1.35 MPa were measured using the Autochem 2950 HP system (Micromeritics, USA). Methane adsorption was measured in a 7:3 ratio mixture of He and methane. Prior to adsorption measurements, the adsorbents were dried under Ar flow at 200 °C for at least 2 hours. The samples were cooled down to the adsorption temperature, the pressure was increased to the desired level and stabilized for at least 30 minutes for each pressure point for measurements. Next, the sample was heated for 10 minutes to 400 °C to measure the amount of adsorbed gas. The volume of adsorbed methane was calcu-

lated with the Peng and Robinson equation of state [130] using Prode software (Milano, Italy). The total amount of adsorbed methane, n_{ads}, was calculated from excess adsorption, n_{exc}, using a modified Langmuir isotherm (Eqs. 2, 38 and 39). Other isotherm models (Toth [136], Temkin [137], Sips (Langmuir-Freundlich) [135], two-Langmuir combination equation (dual-site Langmuir) [156] and Unilan [60]) were also used to calculate the n_{ads}. Single-site Langmuir isotherm gave the best fits of the system, whilst the results from other models reduced back to the single-site Langmuir isotherm equation form. For example, parameter values of $n_{het} = 1$ and $t_{het} = 1$ were obtained from fitting with Sips and Toth equations, respectively, which reduced the Sips and Toth isotherm equations to the Langmuir isotherm equation.

6.8. Electrode materials

"Busofit" carbon fabrics T-1-040, T-040 and L-0.3-135 (OJSC "Svetlogorsk-Khimvolokno", Belarus) were used as electrodes for EDLCs. The carbon fabrics have been synthesized by carbonization of rayon technical filament yarn and activated with water vapour.

Titanium carbide derived carbon (TiC-CDC 950 °C) was synthesized by chlorination of TiC at 950 °C, which is brought in detail under the description of carbide-derived carbon synthesis. The TiC-CDC 950 °C based electrodes were made up of 93 wt% of TiC-CDC 950 °C and 7 wt% of polytetrafluoroethylene (PTFE) binder. PTFE binder was added to TiC-CDC 950 °C as a 2.5 wt% water dispersion diluted from 60 wt% PTFE dispersion in water (Sigma Aldrich), mixed thoroughly and dried at 120 °C and 12 kPa for 24 h. A uniform electrode was produced by roll-pressing hexane-wetted electrode material for multiple times. The roll-pressed electrode was dried at 120 °C and 12 kPa for 24 h.

The average thickness of the used electrodes has been measured with a micrometre thickness gauge (Eee, Taiwan, digital thickness gauge 0-10 mm * 0.001 mm) and thicknesses are given in Table 2.

6.9. Electrochemical measurement and analysis

All investigated electrode materials were sputtered with 2 ± 1 μm Al layer on one side to achieve better contact between the electrode and the current collector. Electrochemical measurements were performed in a symmetrical two-electrode Al test-cell (Hohsen Corp, Japan), which were assembled inside a glove box filled with Ar atmosphere (H_2O and O_2 < 0.1 ppm) at room temperature (21 ± 1 °C). A 25 μm thick cellulose separator TF4425 (Nippon Kodoshi, Japan), two 2 cm^2 disk electrodes, and 3 ml of 1 M triethylmethylammonium tetrafluoroborate ($TEMABF_4$, Stella, 99.9%) in acetonitrile (AN, Sigma-Aldrich, ≥ 99.9%) electrolyte were used to complete the test cell. 3 ml of

1-ethyl-3-methylimidazolium tetrafluoroborate ($EMImBF_4$, Fluka, ≥ 99.0%) was used as the electrolyte with the investigated electrode materials for comparison of carbon fabric properties influence on the electrochemical performance of EDLCs in previous publications [107–109]. To assure the wetting of the electrode material the assembled test cells were cycled between 0 and 1.0 V with 10 mV s^{-1} scan rate for 16 hours prior to electrochemical measurements. The electrochemical behaviour of the supercapacitors was tested using CV and EIS methods on an electrochemical testing station Parstat MC 1000 (Princeton Applied Research, USA). Impedance spectra were measured over alternating current (AC) frequency, *f*, range from 10^{-3} Hz to 3×10^5 Hz with 5 mV amplitude. All gravimetric values are calculated per the whole electrode mass, i.e. mass normalisation is not done only for the active carbon.

7. RESULTS

7.1. Electrochemical measurements of carbon fabric and carbide-derived carbon electrodes

The addition of small organic solvent additions to ionic liquids and ionic liquid mixtures as electrolytes for EDLC applications were studied previously [107–109]. Although the physical properties, conductivity, viscosity, and melting temperature, were improved by the organic solvent addition, the electrochemical performance of EDLC systems could not be remarkably improved by the small addition of organic solvent. Thus, instead of improving the electrolyte, through the addition of components with favourable properties, the influence of carbon electrodes properties on the performance of EDLC systems was taken under investigation. As the carbon fabric electrodes performed comparatively well for electrode material with no dead-mass, i.e. no binder addition, further microporous carbon fabrics were chosen.

TiC-CDC 950 °C and commercial carbon fabric electrodes; L-0.3-135, T-1 and T-1-040, exhibit specific surface areas over 500 m^2 g^{-1} and total pore volumes over 0.25 cm^3 g^{-1} (Table 1 and Table 2). For all the used electrode materials pore widths under 2 nm are prevalent and L-0.3-135 exhibits the smallest pores, with almost all pores with widths under 0.8 nm (Figure 2). As the investigated $TEMABF_4$ electrolyte ions have a minimal diameter without a solvate layer [157,158], the specific surface areas of pores with widths over 0.7 nm are calculated using the 2D-NLDFT-HS model in Table 2. The pore size distribution of TiC-CDC 950 °C powder and TiC-CDC 950 °C made into electrodes are almost identical, where only the specific surface area and pore volume decrease equally with the mass addition of the binder, thus, only the pore size distribution of TiC-CDC 950 °C powder is shown in Figure 2.

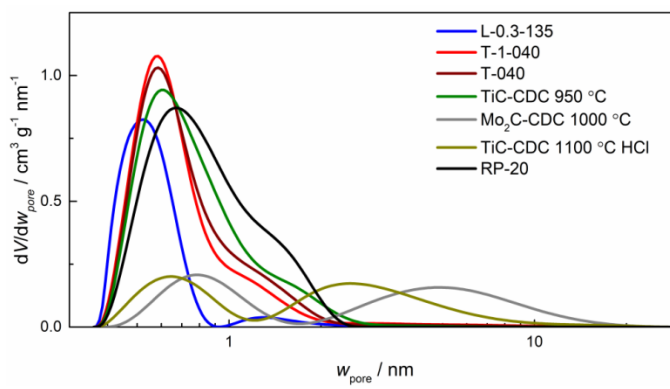

Figure 2. The pore size distribution, the differential volume of pores vs pore width on the axes, for all investigated carbon materials. Pore size distributions have been calculated from the simultaneous fitting of N_2 and CO_2 isotherm data with the 2D-NLDFT-HS model using SAIEUS software.

According to the analysis of Raman spectra, the carbon fabric electrodes are within a similar level of order, with average correlation lengths, L_a, within 16.5 ± 2.1 nm (Table 3). The TiC-CDC 950 °C electrode is more disordered in comparison to the carbon fabrics, with L_a = 8.2 nm.

Based on XPS measurements data carbon fabric L-0.3-135 has the largest amount of surface impurities containing oxygen and silicon (Table 4). The other two carbon fabrics have negligible amount of impurities.

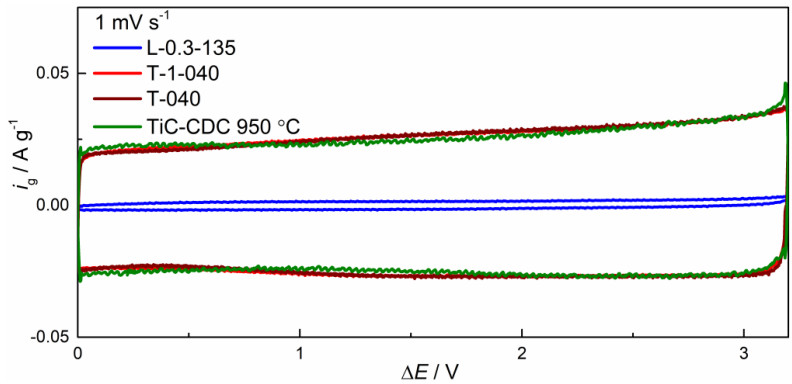

Figure 3. Cyclic voltammograms of 1 M $TEMABF_4$ in AN electrolyte for investigated electrode materials measured at scan rate 1 mV s^{-1}. Current is normalized to the total mass of electrodes.

Cyclic voltammograms measured up to ΔE = 3.2 V and at scan rate of 1 mV s^{-1} are presented in Figure 3. For all electrodes, except L-0.3-135, the current starts to increase nearly exponentially when cell potential higher than 2.8 V is applied. The current for a cell with L-0.3-135 electrodes started to increase nearly exponentially already at ΔE = 2.5 V scan rates, v < 10 mV s^{-1}, were used.

The electrochemical impedance spectroscopy (EIS) measurement at low frequencies and high applied cell potentials, $\Delta E \geq$ 3.2 V exhibit a phase angle more negative than -83° for T-1-040 and T-040 electrodes (Figure 4(a)). The phase angle, ϕ, at ΔE = 2.0 V is near -80° for L-0.3-135. With the increase of ΔE the absolute phase angle value of L-0.3-135 electrodes decreases at low frequencies, whilst maintaining a more negative phase angle, ϕ < -70°, when 0.01 Hz < f < 0.4 Hz (Figure 4(b)).

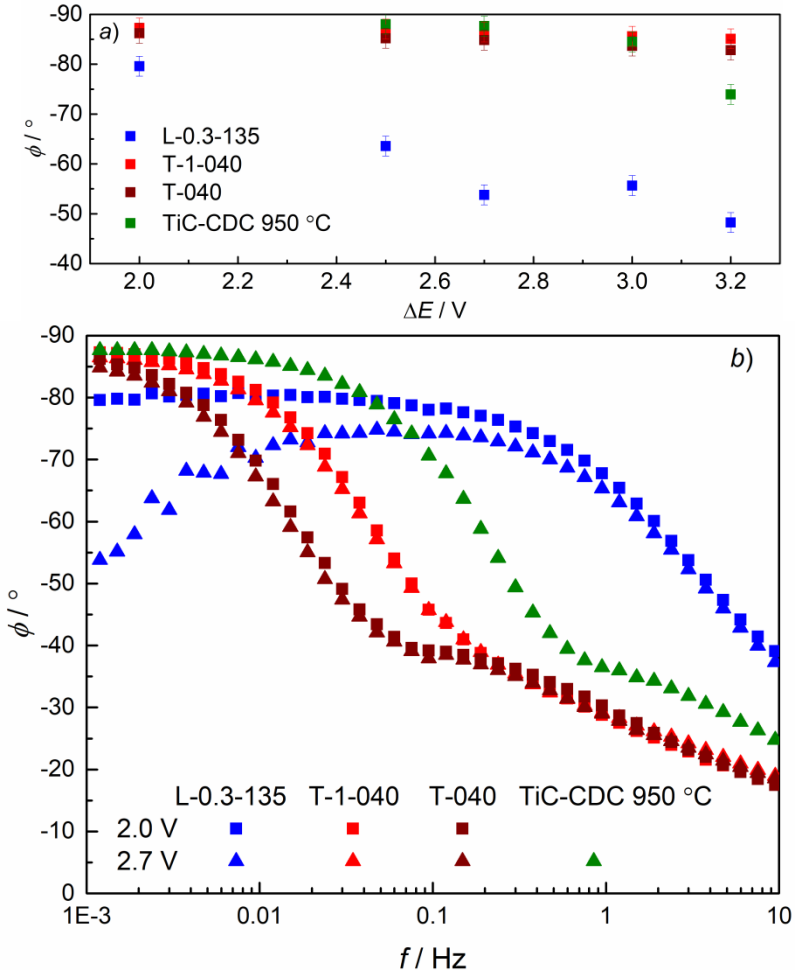

Figure 4. Phase angles (ϕ) of investigated electrode materials with 1 M $TEMABF_4$ in AN electrolyte (a) at various applied cell potentials ΔE (noted in Figure) calculated from EIS measurements at 1 mHz and (b) over a frequency range from 1 mHz up to 10 Hz at two applied cell potentials, given in Figure (2.0 V, squares, and 2.7 V, triangles) (b).

Thus, the applicable cell potential region for T-040 and T-1-040 two-electrode cells filled with 1 M $TEMABF_4$ in AN electrolyte is at least 2.7 V. Only slow Faradic side processes appear at $2.7 < \Delta E \leq 3.2$ V, whereas the applicable cell potential range for L-0.3-135 based cell is only 2.0 V. This is most likely caused by the Si and O surface impurities determined with XPS (Table 4). The impurities start to react with the electrolyte at lower ΔE in comparison to other investigated electrode materials free from contaminants.

Specific capacitance values per one electrode calculated from CV and EIS measurements at 1 mV s^{-1} and at 1 mHz, respectively, are given in Table 4. Investigated electrode materials, except L-0.3-135, have specific capacitance values of $C_{g,1el} \geq 100$ F g^{-1}. L-0.3-135 electrode exhibits a very low capacitance value of $C_{g,1el} < 4$ F g^{-1} and the calculated maximum specific energy density of only $E_{max} = 0.42$ Wh kg^{-1} at 2.0 V (Table 5). In comparison, other electrode materials exhibit E_{max} 28 Wh kg^{-1} at 2.7 V.

Table 5. Electrochemical characteristics of investigated carbon fabrics and TiC-CDC 950 °C electrodes with 1 M $TEMABF_4$ in AN electrolyte. Electrochemical characteristics for L-0.3-135 are acquired at $\Delta E = 2.0$ V and for other electrodes at $\Delta E = 2.7$ V.

Electrode material	$C_{g,1el}$ F g^{-1}	R_s Ω cm^2	C_s F g^{-1}	τ_r s	E_{max} Wh kg^{-1}	P_{max} kW kg^{-1}
L-0.3-135	3.6	0.4	3.0	0.028	0.42	33
T-040	100	0.5	110	4.3	28	46
T-1-040	101	0.5	110	1.6	28	75
TiC-CDC 950 °C	101	0.2	108	0.4	27	218

$C_{g,1el}$ –specific capacitance calculated from the averaged discharge current from CV measurements at 1 mV s^{-1}, R_s – series resistance calculated from EIS data at $Z'' = 0$ Ω cm^2, C_s – series capacitance per one electrode at 1 mHz calculated from EIS data according to equation (23), τ_r – characteristic relaxation time calculated from intersection frequency of real and imaginary part of complex power components according to Eq. 32, E_{max} – maximal specific energy per total electrode mass (according to Eq. 26), P_{max} – maximal specific power per total electrode mass (according to Eq. 27).

$TEMA^+$ ions linear dimensions are between 0.65 and 0.8 nm, depending on the direction [157,158] and most pores in L-0.3-135 are smaller than 0.8 nm. Thus, the very low capacitance and energy density values are caused by the size restrictions of the small pores in the electrode material, where the electrolyte ions have limited access to the electrode surface area (Table 2).

The TiC-CDC 950 °C electrodes do not exhibit higher capacitance values if compared with T-040 and T-1-040, regardless of the larger available surface area in comparison to other investigated electrode materials. This limited increase in the amount of stored energy with the increase of specific surface area is in accordance with results by other authors and is explained by the limited charge the carbon material can acquire when the pore walls, i.e. carbon density, get thinner with the increase in porosity and specific surface area [13,18].

The relaxation time constant, τ_r, and the maximum specific power, P_{max}, (Table 5) are in complex dependence with the properties of the electrode material, i.e. τ_r and P_{max} are influenced by the thickness of the electrode, size of the pores, and the conductivity of the electrode material [159–161]. The T-1-040 and T-040 electrodes have almost identical pore size distributions, specific surface areas, average correlation lengths, amount of surface impurities, and series resistances. Thus, the almost threefold difference in τ_r and the one and a half times difference in P_{max} between T-1-040 and T-040 can be explained by the differences in the electrode thickness, where the thinner electrode has higher P_{max} and smaller τ_r. In respect to practical applications, the quick τ_r and adequate P_{max} of L-0.3-135 are counteracted by the lacking amount of stored energy. The two magnitudes quicker τ_r of L-0.3-135 in comparison to the other two carbon fabrics indicates that the electrical double layer forms only on the external surface of the electrode material as the pores are not accessible to the electrolyte ions. The outstanding P_{max} for TiC-CDC 950 °C is achieved through a combination of higher conductivity (lower R_s), the higher contribution of pores with widths > 1 nm, and the low thickness of the electrode material.

Otherwise identical EDLCs were assembled with $EMImBF_4$ electrolyte. The objective was to compare the investigated carbon fabrics properties influence on electrochemical performance with previously used microporous carbon cloth (MPCC) electrode [107–109]. In comparison to the investigated electrode materials (Table 1) MPCC is a high surface area (S_{BET} = 1560 m^2 g^{-1}) binderless electrode material with a substantial amount of pores with widths over 2 nm (V_{micro}/V_{tot} = 0.75 and S_{micro}/S_{BET} = 0.93). All investigated electrode materials, except L-0.3-135, exhibited almost ideally capacitive behaviour at applied cell potential ΔE = 3.2 V based on cyclic voltammograms (Figure 5). Similarly to 1 M TEMABF4 in AN electrolyte, the $EMImBF_4$ ionic liquid electrolyte exhibits a very low capacitance (3.8 F g^{-1}, Table 6) with L-0.3-135 electrode, which is caused by the lacking amount of pores with widths larger than 0.8 nm and the large ionic radius of $EMIm^+$, 3.04 Å [162]. The considerable ratio of pores with pore widths over 2 nm (Pore size distribution presented in [108]) in MPCC electrodes brings forth the enhanced power performance in comparison to other investigated carbon fabric electrode materials. This is exhibited by the more rectangular-shaped voltammograms of MPCC electrodes at scan rate 1 mV s^{-1} in comparison to other investigated carbon fabric electrodes (Figure 5).

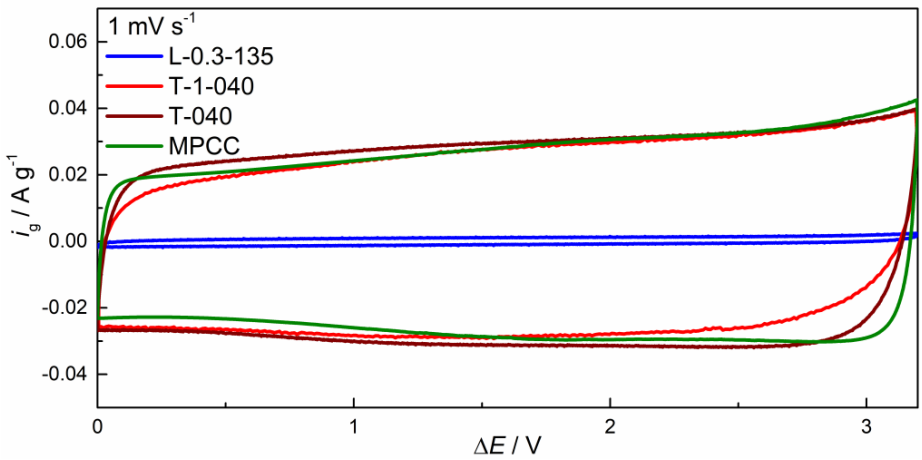

Figure 5. Cyclic voltammograms of $EMImBF_4$ electrolyte for investigated carbon fabric electrode materials and MPCC electrode material [107–109] measured at scan rate 1 mV s^{-1}. Current is normalized to the total mass of electrodes.

Regardless of the larger thickness of MPCC electrodes (0.78 mm, Table 6), the τ_r of $EMImBF_4$ electrolyte with MPCC electrodes was lower than for T-040. In case of $EMImBF_4$ electrolyte the difference in the surface area from large enough pores, $S_{DFT0.7nm}$, between T-040 and T-1-040 is apparent in the higher specific calculated capacitance, $C_{g,1el}$, of T-040 (Table 6). The higher R_s of MPCC electrodes is most probably caused by the larger thickness of MPCC electrodes (Table 6).

Table 6. Electrochemical characteristics of investigated carbon fabrics electrodes with $EMImBF_4$ electrolyte. Electrochemical characteristics are acquired at ΔE = 3.2 V.

Electrode material	**Thickness mm**	$C_{g,1el}$ **F** g^{-1}	R_s **Ω** cm^2	τ_r **s**	**Origin of data**
L-0.3-135	0.42 ± 0.02	3.8	0.9	0.078	This work
T-040	0.38 ± 0.02	115	0.9	57	This work
T-1-040	0.25 ± 0.02	101	1.0	6.9	This work
MPCC	0.78	107	1.8	17	[107–109]

$C_{g,1el}$ –specific capacitance calculated from the averaged discharge current from CV measurements at 1 mV s^{-1}, R_s – series resistance calculated from EIS data at Z'' = 0 Ω cm^2, τ_r – characteristic relaxation time calculated from intersection frequency between the real and the imaginary part of complex power components according to Eq. 32.

The electrochemical investigation of the three carbon fabric electrodes and one carbide-derived carbon electrode demonstrated the fundamental aspects of using carbon-based materials as electrical double layer capacitor electrodes. The uselessness of carbon electrodes with too small pores in comparison to the electrolyte ion size is shown by the limited capacitance values of L-0.3-135 as has been shown for C-SiC (without activation) two-electrode cells [119]. In case of sufficiently large pores, the capacitance does not increase over a climiting value, even when available specific surface area increases. This is exhibited by the limited capacitance values of electrodes made from TiC-CDC 950 °C, although the available specific surface area is larger than for T-1-040 and T-040 electrodes. The influence of electrode thickness is exhibited by the otherwise identical electrodes T-1-040 and T-040, where thinner electrode shows almost twice the power performance (power density) in comparison to the thicker electrode. The enhanced power performance in the presence of larger pores is exhibited by the TiC-CDC 950 °C electrode. The importance of larger pores for the effective diffusion of electrolyte ions is shown with the ionic liquid, $EMImBF_4$, electrolyte and through the comparison with previous publications [107–109].

7.2. Methane adsorption on carbide-derived carbons

The adsorption of methane is investigated on three carbide-derived carbons (CDCs), TiC-CDC 950 °C, TiC-CDC 1100 °C HCl and Mo_2C-CDC 1000 °C. The pore size and the level of ordering of the carbon structure increase in the following order: TiC-CDC 950 °C < TiC-CDC 1100 °C HCl < Mo_2C-CDC 1100 °C, according to the V_{micro}/V_{tot} (Table 1), the pore size distribution (Figure 2). The L_a and I_D/I_G values are given in Table 3.

The isotherm of the total amount of adsorbed methane is calculated by fitting a modified Langmuir isotherm on the methane excess adsorption isotherms (Figure 6). The maximum adsorption, n_{ads}^{max}, calculated from the modified Langmuir isotherm fit at isothermal conditions, is highest for TiC-CDC 950 °C system at all measured temperatures (Figure 7 (a)). The n_{ads}^{max} is normalized with the specific surface areas, calculated by using the BET theory, S_{BET}, and by using the DFT modelling, S_{DFT}, method (Table 1 and Table 2) to compare the amount of methane that can adsorb per unit of surface area (Figure 7 (b,c)). The n_{ads}^{max} values normalized with the specific surface area, except TiC-CDC 1100 HCl normalized with S_{BET}, are within uncertainty limits of each other. The unreliability associated with using the BET theory on N_2 adsorption isotherms, especially in the case of microporous adsorbents, has been brought up and discussed in Ref. [163]. In addition, the n_{ads}^{max} of TiC-CDC 1100 HCl normalized with S_{DFT}, which combined both N_2 and CO_2 adsorption isotherms, falls

in line with other adsorbent n_{ads}^{max} values normalized with S_{DFT}. Thus, the n_{ads}^{max} per surface area is almost equal in case of investigated carbon materials, i.e. the maximum amount of methane that can be adsorbed per unit of surface area does not remarkably vary in the range of investigated specific surface areas (from 700 $m^2 g^{-1}$ up to 1500 $m^2 g^{-1}$) and pore size distributions (Figure 2).

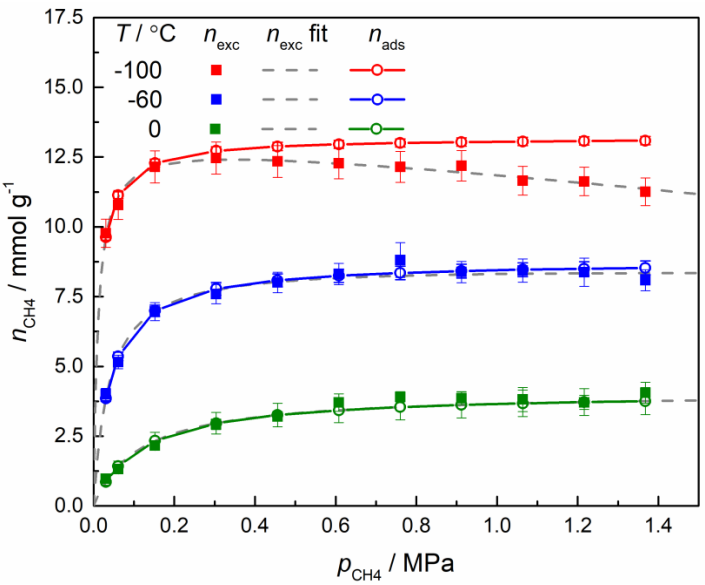

Figure 6. Measured excess adsorption (squares, filled), excess adsorption fit with the modified Langmuir isotherm (dashed grey lines) and the calculated total adsorption isotherm (circles, empty filling) of methane on TiC-CDC 950 °C at three different temperatures, noted in Figure.

The equilibrium coefficients of methane adsorption, *K*, calculated from the fitting with modified Langmuir isotherm fit, are presented in Figure 7 (d). Calculated *K* values decrease in the following order: TiC-CDC 950 °C > TiC-CDC 1100 °C HCl > Mo_2C-CDC 1000 °C. A higher *K* value means that adsorption is more favoured at a certain pressure and temperature, i.e. with an increase in *K* the same fraction of the surface of the adsorbent is covered with adsorbed species at lower pressures. Thus, the pressure of methane adsorption is lower on CDCs with smaller pores and with lower average correlation lengths, L_a.

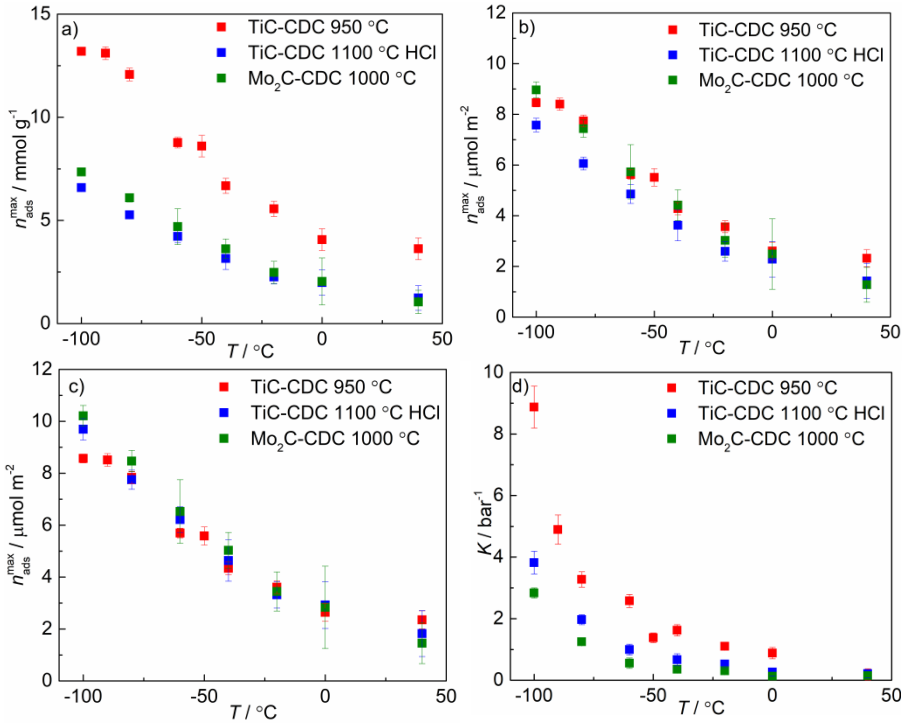

Figure 7. Gravimetric maximum adsorption of methane (a), maximum adsorption of methane normalized with the BET specific surface area (b), maximum adsorption of methane normalized with the DFT specific surface area (c) and the methane adsorption coefficient (d) of the three investigated CDC adsorbents. All data is obtained from the fitting of n_{exc} with a modified Langmuir isotherm (Eq. 2, 38 and 39).

The adsorption enthalpy, ΔH_{ads}^{Θ}, and adsorption entropy, ΔS_{ads}^{Θ}, of methane are calculated at standard state (0.1 MPa, i.e. 1 bar) by the use of the Van't Hoff equation (Figure 8) to gain a better understanding of the effect of the CDC adsorbents surface on the adsorption thermodynamics. The ΔS_{ads}^{Θ} decreases towards more negative values with the increase in L_a and with the increase of pore size according to the pore size distribution data (Figure 2). The same trend can be seen for ΔH_{ads}^{Θ}, although not in such a conclusive manner. As the L_a decreases, i.e. the disorder of material increases in the CDC materials, a larger amount of edge and/or defective sites in the graphitic carbon structure are available for adsorption of methane. Thus, the adsorbed methane forms a less ordered adsorption layer, i.e. the absolute value of the entropy of adsorption is smaller. The formation of a more uniform layer of adsorbed methane causes a more negative enthalpy of adsorption, where the enthalpy of adsorption goes towards more positive values with the use of a more ordered CDC adsorbent. As the entropy of adsorption in the Gibbs free energy equation (Eq. 47) is

multiplied with temperature, the more positive entropy of adsorption is especially beneficial for adsorption of methane at higher temperatures but bestows limited advantage at low temperatures, e.g. near the temperature of methane liquefaction (90.7 K). Thus, in case of the investigated CDCs (T < 130 K, i.e. T < -143 °C) the enthalpy of adsorption, for attaining favourable adsorption equilibrium, is crucial only at very low temperatures.

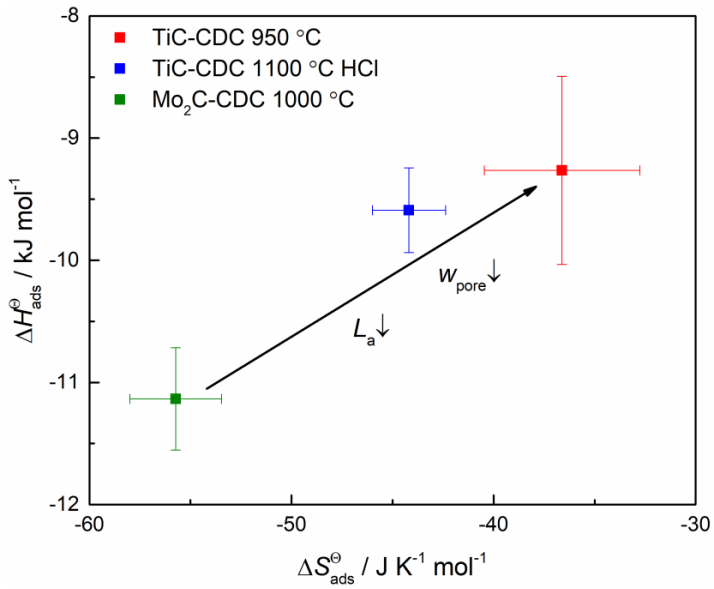

Figure 8. The enthalpy and entropy of methane adsorption in standard state at investigated CDC adsorbents. The arrow indicates the decrease in the average pore size and in the average correlation length for the CDC adsorbents.

Based on the adsorption measurements of methane on three CDCs the maximum amount of adsorbed methane per surface area at isothermal conditions does not remarkably depend on the pore size or the level of ordering of the carbon materials under investigation. The adsorption equilibrium is notably influenced by the carbon structure and adsorption of methane on more disordered and more microporous CDCs has a more positive adsorption entropy and enthalpy. Thus, by using carbon materials with a higher level of disorder and/or with smaller pores the same fractional surface coverage can be achieved at much lower pressures (Figure 9), especially at higher temperatures ($T \geq$ -60 °C).

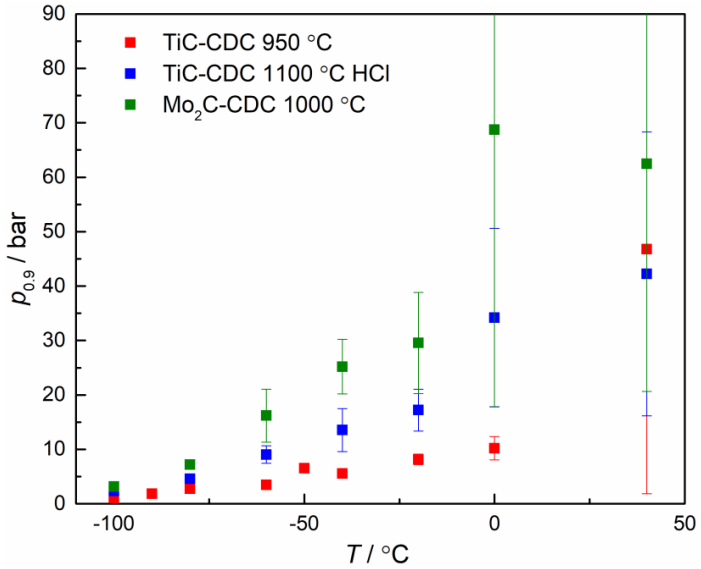

Figure 9. The pressure at which the fractional surface coverage, θ, is 0.9, i.e. n_{ads} is 90% from the n_{ads}^{max}, vs. the temperature of adsorption for investigated CDC adsorbents.

7.3. Complex metal hydride/carbon composites

Commercial carbon RP-20 is used as the supporting material for confining $NaAlH_4$. RP-20 is a microporous carbon (most pores with widths < 2 nm) (Figure 2) with a high surface area (S_{BET} = 1840 m^2 g^{-1} and S_{DFT} = 1650 m^2 g^{-1}) (Table 1 and 2). Based on the L_a value of 16.1 nm (Table 2), calculated from Raman spectra, RP-20 is ordered carbon in relation to CDCs.

The presence of crystalline $NaAlH_4$ is determined by X-ray diffraction (XRD) for all $NaAlH_4$/RP-20 composite materials with ≥ 10 wt% of $NaAlH_4$ (Figure 10, Table 7). Thus, even at low wt% of $NaAlH_4$ some of the $NaAlH_4$ is deposited as a bulk/crystalline phase. The decomposition and hydrogen release temperature of $NaAlH_4$ is lowered through the confinement of low wt% of $NaAlH_4$ in a carbon scaffold. The bulk $NaAlH_4$ started releasing H_2 at 170 °C but the 10$NaAlH_4$/RP-20 started releasing H_2 already near ambient temperature (< 40 °C), (Figure 11).

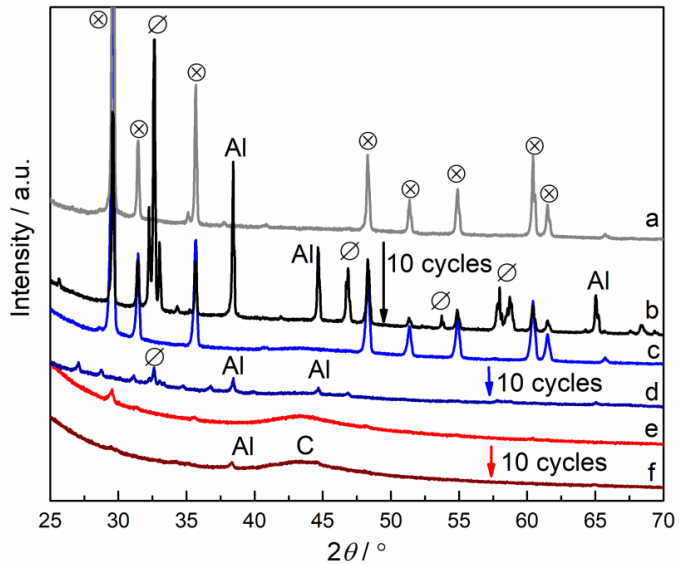

Figure 10. X-ray diffractograms of bulk $NaAlH_4$ (a, b), $60NaAlH_4$/RP-20 (c, d) and $10NaAlH_4$/RP-20 (e, f) before (a, c and e) and after 10 dehydrogenation/hydrogenation cycles (b, d and f). Diffraction peaks of $NaAlH_4$ are noted as ⊗ and diffraction peaks of Na_3AlH_6 are noted as ∅.

Table 7. The average crystallite sizes and hydrogen content of pure $NaAlH_4$ and $NaAlH_4$/RP-20 composite materials

$NaAlH_4$ wt%	**Cycled**	**τ($NaAlH_4$) nm**	**τ(Al) nm**	**τ(Na_3AlH_6) nm**
100	No	110 ± 2		
100	Yes, at 200 °C	95 ± 3	201 ± 10	165 ± 7
60	No	76 ± 2		
60	Yes, at 200 °C		146 ± 14	207 ± 42
10	No	47 ± 5		
10	Yes, at 170 °C		50 ± 7	

τ – Average crystalline domain size of $NaAlH_4$, Al and Na_3AlH_6.

10 dehydrogenation/hydrogenation cycles (cycling) are performed to determine the effect of confinement on the ability of $NaAlH_4$ to release hydrogen reversibly. Diffraction peaks from decomposition products, Al and/or Na_3AlH_6, appear for bulk $NaAlH_4$ and for all cycled $NaAlH_4$/RP-20 composites (Figure 10). After cycling the $NaAlH_4$ diffraction peak is only detected for bulk $NaAlH_4$. Thus, confined $NaAlH_4$ does not reform as a crystalline with large enough crystallites to be detectable with XRD after cycling. The calculated average crystallite sizes are given in Table 7. The decomposition products, Al

and Na_3AlH_6, form larger crystallites during cycling in comparison to the primary $NaAlH_4$, with the exception of 10$NaAlH_4$/RP-20. The equal size of Al crystallites after cycling and $NaAlH_4$ crystallites before cycling in 10$NaAlH_4$/ RP-20 is most likely caused by the limited segregation of Al into larger crystallites, which is withheld by more effective confinement of $NaAlH_4$, when lower wt% os $NaAlH_4$ is deposited onto/into RP-20.

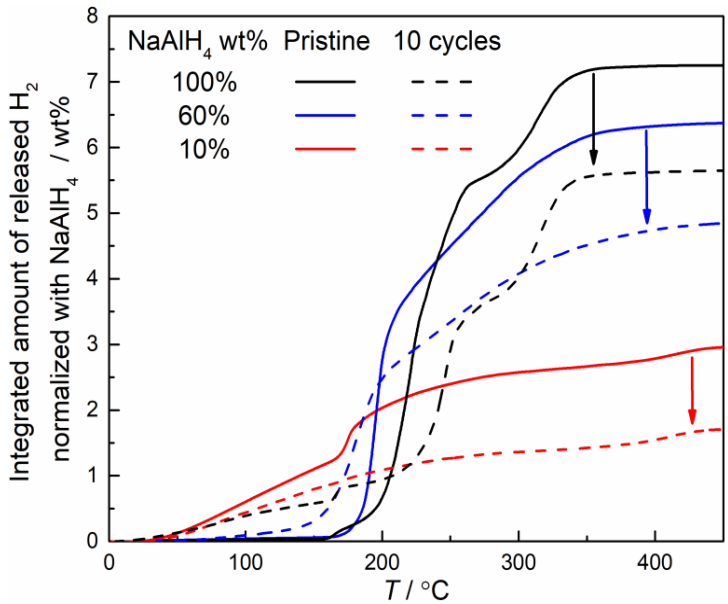

Figure 11. Integrated wt% of released hydrogen from bulk $NaAlH_4$ (black line), from 60$NaAlH_4$/RP-20 (blue line) and from 10$NaAlH_4$/RP-20 (red line) before (filled lines) and after 10 dehydrogenation/hydrogenation cycles (dashed lines). Released hydrogen is measured with an applied temperature ramp rate of 2 °C min^{-1}.

Substantial degradation in the amount of released hydrogen is observed for all materials after cycling (Figure 11). During cycling at 200 °C the intensive hydrogen release temperature for bulk $NaAlH_4$ shifted from 220 °C to 245 °C. Meanwhile, the total amount of released hydrogen is not reduced in a larger degree in comparison to $NaAlH_4$/RP-20 composite materials. This might be caused by the merging of $NaAlH_4$ into a unitary bulk at melting temperature, which kinetically hinders the hydrogen release and, thus, hydrogen is released at higher temperatures when a constant temperature ramp-up rate is applied. Nevertheless, the reversible decomposition/reformation of $NaAlH_4$ is maintained. In contrast to bulk $NaAlH_4$, the temperature of the intensive hydrogen release from 60$NaAlH_4$/RP-20 is decreased from 195 °C to 180 °C and the

the intensive hydrogen release during cycling of confined $NaAlH_4$ is caused by the conversion of $NaAlH_4$ crystallites, i.e. ordered particles, into more amorphous and/or smaller particles, which is supported by the disappearance of the $NaAlH_4$ diffraction peak during continuous cycling.

It is shown that the confinement of $NaAlH_4$ onto/into a supporting carbon material decreases the temperature of hydrogen release. Hydrogen is released already at ambient temperature in case of low wt% loading of $NaAlH_4$ into RP-20. Confinement of $NaAlH_4$ into RP-20 prevents the formation of larger $NaAlH_4$ crystallites during cycling and, thus, keeps/decreases the temperature of hydrogen release.

In principle, confinement of $NaAlH_4$ should also increase the amount of reversibly released hydrogen. However, this is not the case as the ratio of reversibly stored hydrogen is nearly equal for all investigated materials. Also, Al diffraction peaks, from the irreversible decomposition of $NaAlH_4$, appear for all investigated materials. In addition to the contribution from the segregation of decomposition products to the decrease in the amount of reversibly stored hydrogen, the inherent stability of nanoconfined $NaAlH_4$ into RP-20 might decrease the amount of released hydrogen. The hydrogenated samples are stored, between the cycling and the hydrogen release measurements, in Ar atmosphere and at ambient conditions. It was found that the $10NaAlH_4$/RP-20 starts to release hydrogen already near ambient temperature. Thus, the $10NaAlH_4$/RP-20 material might have decomposed already between the cycling and hydrogen release measurements.

7.4. Conclusion

The gas adsorption, electrochemistry, and investigations into the capability of carbon composite material to hydrogen storage are implemented to investigate the influence of carbon materials properties on the energy storage applications.

The amount of stored energy, charge in case of electrical double layer capacitor (EDLC) systems and molecules of gas in case of physical adsorption, per surface area depends on chemical nature of the adsorbing species. In case of molecular adsorbents the maximum amount (which can be adsorbed) depends linearly on the surface area, i.e. at isothermal conditions the number of adsorbed molecules at full surface coverage per surface area is constant, regardless of the pore size and specific surface area values. For charged adsorbates, i.e. ionic species, there is a limit to how many ions contribute to the formation of electrical double layer (EDL) at a certain applied cell potential. When available surface area increases over a limiting value, the additional surface area does not increase the amount of charge stored in an EDL. This is caused by the limited amount of carbon available to charge in case of high surface area materials and the repulsive interactions between adsorbed ions with the same charge type. Thus, to increase the amount of adsorbed gas in the porous material a maximum possible surface area should be pursued, but for an increased amount of stored

electric charge in the EDL alternative methods should be applied, such as surface functionalisation, alternative materials to carbon etc.

The influence of the pore size of a carbon material on the energy storage applications is most critical in case of systems where the liquid phase molecules and ions diffusion rate is a limiting step to achieve higher power densities. The increased power density of TiC-CDC 950 °C electrodes is, in addition to the smaller thickness, enhanced by the presence of somewhat larger pores in the hierarchical porous structure. As both the level of ordering and pore size depend on the carbide-derived carbon (CDC) used to investigate the adsorption of methane, both must be taken into account at the same time. The thermodynamics of methane adsorption, i.e. enthalpy and entropy of adsorption, is more favoured in case of smaller pore size and lower average correlation length, i.e. depending on the level of graphitic ordering of CDCs. Thus, adsorbents with higher disorder and smaller pores adsorb the same amount of gases at lower pressures.

The capability of microporous carbon to confine the complex metal hydride into carbon structure and, thus, lower the temperature of hydrogen release has been shown. Most remarkably, confinement of < 60 wt% $NaAlH_4$ onto/into microporous carbon, RP-20, depresses the segregation of decomposition products, thus, improving the reversible hydrogen storage capability of $NaAlH_4$/RP-20 over more usage cycles. In addition, the confinement of $NaAlH_4$ into/onto microporous carbon caused the reforming of $NaAlH_4$ into smaller particles or as an amorphous state during the implementation of multiple dehydrogenation/hydrogenation cycles.

8. SUMMARY

The influence of the properties of carbon materials on the behaviour of energy storage applications was investigated using microporous carbon materials with the high sruface area. Carbon materials were used as electrode materials in electrical double layer capacitors (EDLCs) for electrical charge storage, as gas adsorbents for adsorption of methane, and as a supporting material for hydrogen storage in nanoconfined complex metal hydride. The main properties of interest for the carbon materials were specific surface area and the amount of stored energy per active surface area, average pore size and pore size distribution, and level of ordering (average correlation length). The specific surface areas, the volume of pores, and the pore size distribution of investigated carbon materials were determined with N_2 and CO_2 adsorption methods. The average correlation length was determined fitting the Raman spectra.

Electrochemical measurements were performed on three carbon fabrics and one carbide-derived carbon (CDC) based electrode material with organic solvent based electrolyte, 1 M triethylmethylammonium tetrafluoroborate ($TEMABF_4$) in acetonitrile (AN), and with the ionic liquid, 1-ethyl-3-methylimidazolium tetrafluoroborate ($EMImBF_4$). The carbon electrode materials were covered with an Al layer, for improved conductivity, and the electrode thicknesses were measures. The unsuitability of pores with too small widths, in comparison to the electrolyte ions, the influence of electrode thickness to power density and the small influence of increasing the available surface area over a certain value (> 500 m^2 g^{-1}) to the energy density were shown. Also, the larger dependency of energy density on the available surface area in case of an ionic liquid electrolyte, $EMImBF_4$, in comparison to 1 M $TEMABF_4$ in AN electrolyte was shown.

Methane adsorption was investigated on three CDC adsorbent materials with different and well-defined pore size distributions and average correlation lengths. The excess adsorption isotherms of methane were measured at methane partial pressures from 0.03 to 1.35 MPa and at temperatures from -100 °C to 40 °C. The total adsorption isotherms were calculated from fitting the excess adsorption isotherms with a modified Langmuir isotherm equation. The adsorption enthalpy and entropy were calculated according to the Van't Hoff equation from the fitting results with a modified Langmuir isotherm equation. For investigated CDC adsorbent materials the maximum adsorbed amount of methane normalized with the surface area is almost equal, thus, the maximum amount of gas adsorbed does not depend on the pore size or level of ordering in the case of investigated CDCs. In the adsorption equilibrium, adsorption is more favoured in the case of more disordered CDCs with smaller pores.

Microporous high surface area carbon, RP-20, was used as a supporting material for the nanoconfinement of complex metal hydride $NaAlH_4$. From 10 to 60 wt% of $NaAlH_4$ was deposited onto/into RP-20 through solution impregnation method and the amount of released hydrogen was measured at a

constant temperature ramp rate. The presence and crystallite sizes of $NaAlH_4$ and the decomposition products of $NaAlH_4$ were determined by X-ray diffraction. The temperature, at which hydrogen release started, was lowered from 170 to 40 °C through the nanoconfinement of $NaAlH_4$. 10 dehydrogenation/hydrogenation cycles were applied on the $NaAlH_4$/RP-20 composite materials and pure $NaAlH_4$. The temperature of hydrogen release decreased during cycling and the $NaAlH_4$ diffraction peaks were not detectable in case of 60$NaAlH_4$/RP-20. The nanoconfinement of $NaAlH_4$ onto/into a microporous carbon material caused the reforming of $NaAlH_4$ into smaller or more amorphous particles during cycling.

9. REFERENCES

[1] United Nations, Adoption of the Paris Agreement, 21st Conference of the Parties, United Nations, Paris, 2015.

[2] B. Dunn, H. Kamath, J.-M. Tarascon, Electrical Energy Storage for the Grid: A Battery of Choices, Science. 334 (2011) 928–935. doi:10.1126/science.1212741.

[3] H. Ibrahim, A. Ilinca, J. Perron, Energy storage systems—Characteristics and comparisons, Renew. Sustain. Energy Rev. 12 (2008) 1221–1250. doi:10.1016/j.rser.2007.01.023.

[4] K. Agbossou, M. Kolhe, J. Hamelin, T.K. Bose, Performance of a stand-alone renewable energy system based on energy storage as hydrogen, IEEE Trans. Energy Convers. 19 (2004) 633–640. doi:10.1109/TEC.2004.827719.

[5] L. Schlapbach, A. Züttel, Hydrogen-storage materials for mobile applications, in: Mater. Sustain. Energy, Co-Published with Macmillan Publishers Ltd, UK, 2010: pp. 265–270. doi:10.1142/9789814317665_0038.

[6] A.A. Balandin, Thermal properties of graphene and nanostructured carbon materials, Nat. Mater. 10 (2011) 569. doi:10.1038/nmat3064.

[7] M.A. Tamor, W.C. Vassell, Raman '"fingerprinting"' of amorphous carbon films, J. Appl. Phys. 76 (1994) 3823–3830. doi:10.1063/1.357385.

[8] J. Robertson, Amorphous carbon, Adv. Phys. 35 (1986) 317–374. doi:10.1080/00018738600101911.

[9] E. Frackowiak, F. Béguin, Carbon materials for the electrochemical storage of energy in capacitors, Carbon. 39 (2001) 937–950. doi:10.1016/S0008-6223(00)00183-4.

[10] S.L. Candelaria, Y. Shao, W. Zhou, X. Li, J. Xiao, J.-G. Zhang, Y. Wang, J. Liu, J. Li, G. Cao, Nanostructured carbon for energy storage and conversion, Nano Energy. 1 (2012) 195–220. doi:10.1016/j.nanoen.2011.11.006.

[11] D. Lozano-Castelló, J. Alcañiz-Monge, M.A. de la Casa-Lillo, D. Cazorla-Amorós, A. Linares-Solano, Advances in the study of methane storage in porous carbonaceous materials, Fuel. 81 (2002) 1777–1803. doi:10.1016/S0016-2361(02)00124-2.

[12] M. Jordá-Beneyto, F. Suárez-García, D. Lozano-Castelló, D. Cazorla-Amorós, A. Linares-Solano, Hydrogen storage on chemically activated carbons and carbon nanomaterials at high pressures, Carbon. 45 (2007) 293–303. doi:10.1016/j.carbon.2006.09.022.

[13] O. Barbieri, M. Hahn, A. Herzog, R. Kötz, Capacitance limits of high surface area activated carbons for double layer capacitors, Carbon. 43 (2005) 1303–1310. doi:10.1016/j.carbon.2005.01.001.

[14] Y. Zhai, Y. Dou, D. Zhao, P.F. Fulvio, R.T. Mayes, S. Dai, Carbon Materials for Chemical Capacitive Energy Storage, Adv. Mater. 23 (2011) 4828–4850. doi:10.1002/adma.201100984.

[15] J. Chmiola, G. Yushin, R. Dash, Y. Gogotsi, Effect of pore size and surface area of carbide derived carbons on specific capacitance, J. Power Sources. 158 (2006) 765–772. doi:10.1016/j.jpowsour.2005.09.008.

[16] M.G. Nijkamp, J.E.M.J. Raaymakers, A.J. van Dillen, K.P. de Jong, Hydrogen storage using physisorption – materials demands, Appl. Phys. A. 72 (2001) 619–623. doi:10.1007/s003390100847.

[17] R.B. Rios, F.W.M. Silva, A.E.B. Torres, D.C.S. Azevedo, C.L. Cavalcante, Adsorption of methane in activated carbons obtained from coconut shells using

H_3PO_4 chemical activation, Adsorption. 15 (2009) 271–277. doi:10.1007/s10450-009-9174-9.
[18] J. Gamby, P.L. Taberna, P. Simon, J.F. Fauvarque, M. Chesneau, Studies and characterisations of various activated carbons used for carbon/carbon supercapacitors, J. Power Sources. 101 (2001) 109–116. doi:10.1016/S0378-7753(01)00707-8.
[19] H. Shi, Activated carbons and double layer capacitance, Electrochimica Acta. 41 (1996) 1633–1639. doi:10.1016/0013-4686(95)00416-5.
[20] Y. Gogotsi, R.K. Dash, G. Yushin, T. Yildirim, G. Laudisio, J.E. Fischer, Tailoring of Nanoscale Porosity in Carbide-Derived Carbons for Hydrogen Storage, J. Am. Chem. Soc. 127 (2005) 16006–16007. doi:10.1021/ja0550529.
[21] Y. Gogotsi, C. Portet, S. Osswald, J.M. Simmons, T. Yildirim, G. Laudisio, J.E. Fischer, Importance of pore size in high-pressure hydrogen storage by porous carbons, Int. J. Hydrog. Energy. 34 (2009) 6314–6319. doi:10.1016/j.ijhydene.2009.05.073.
[22] D. Lozano-Castelló, D. Cazorla-Amorós, A. Linares-Solano, D.F. Quinn, Influence of pore size distribution on methane storage at relatively low pressure: preparation of activated carbon with optimum pore size, Carbon. 40 (2002) 989–1002. doi:10.1016/S0008-6223(01)00235-4.
[23] C.L. Mangun, M.A. Daley, R.D. Braatz, J. Economy, Effect of pore size on adsorption of hydrocarbons in phenolic-based activated carbon fibers, Carbon. 36 (1998) 123–129. doi:10.1016/S0008-6223(97)00169-3.
[24] D. Qu, H. Shi, Studies of activated carbons used in double-layer capacitors, J. Power Sources. 74 (1998) 99–107. doi:10.1016/S0378-7753(98)00038-X.
[25] J. Chmiola, G. Yushin, Y. Gogotsi, C. Portet, P. Simon, P.L. Taberna, Anomalous Increase in Carbon Capacitance at Pore Sizes Less Than 1 Nanometer, Science. 313 (2006) 1760–1763. doi:10.1126/science.1132195.
[26] N. Jäckel, M. Rodner, A. Schreiber, J. Jeongwook, M. Zeiger, M. Aslan, D. Weingarth, V. Presser, Anomalous or regular capacitance? The influence of pore size dispersity on double-layer formation, J. Power Sources. 326 (2016) 660–671. doi:10.1016/j.jpowsour.2016.03.015.
[27] R. Palm, H. Kurig, T. Romann, U. Joost, R. Kanarbik, R. Väli, I. Tallo, T. Thomberg, A. Jänes, E. Lust, Application of Some Carbon Fabrics as Outstanding Supercapacitor Electrode Materials in Acetonitrile Based Electrolyte, J. Electrochem. Soc. 164 (2017) A453–A460. doi:10.1149/2.0831702jes.
[28] R. Palm, I. Tallo, T. Romann, H. Kurig, Methane adsorption on specially designed TiC and Mo_2C derived carbons with different pore size and surface morphology, Microporous Mesoporous Mater. 218 (2015) 167–173. doi:10.1016/j.micromeso.2015.07.016.
[29] R. Palm, H. Kurig, J. Aruväli, E. Lust, $NaAlH_4$/microporous carbon composite materials for reversible hydrogen storage, Microporous Mesoporous Mater. 264 (2018) 8–12. doi:10.1016/j.micromeso.2017.12.027.
[30] R.C. Bansal, M. Goyal, Activated Carbon Adsorption, CRC Press, 2005.
[31] K.P.D. JONG, J.W. GEUS, Carbon Nanofibers: Catalytic Synthesis and Applications, Catal. Rev. 42 (2000) 481–510. doi:10.1081/CR-100101954.
[32] M. Trojanowicz, Analytical applications of carbon nanotubes: a review, TrAC Trends Anal. Chem. 25 (2006) 480–489. doi:10.1016/j.trac.2005.11.008.
[33] Y. Gogotsi, V. Presser, Carbon Nanomaterials, CRC Press, 2006.

[34] A.C. Ferrari, J. Robertson, Interpretation of Raman spectra of disordered and amorphous carbon, Phys. Rev. B. 61 (2000) 14095–14107. doi:10.1103/PhysRevB.61.14095.
[35] H.K. Chae, D.Y. Siberio-Pérez, J. Kim, Y. Go, M. Eddaoudi, A.J. Matzger, M. O'Keeffe, O.M. Yaghi, A route to high surface area, porosity and inclusion of large molecules in crystals, Nature. 427 (2004) 523. doi:10.1038/nature02311.
[36] H.M. Cheng, F. Li, G. Su, H.Y. Pan, L.L. He, X. Sun, M.S. Dresselhaus, Large-scale and low-cost synthesis of single-walled carbon nanotubes by the catalytic pyrolysis of hydrocarbons, Appl. Phys. Lett. 72 (1998) 3282–3284. doi:10.1063/1.121624.
[37] Y.Z. Jin, C. Gao, W.K. Hsu, Y. Zhu, A. Huczko, M. Bystrzejewski, M. Roe, C.Y. Lee, S. Acquah, H. Kroto, D.R.M. Walton, Large-scale synthesis and characterization of carbon spheres prepared by direct pyrolysis of hydrocarbons, Carbon. 43 (2005) 1944–1953. doi:10.1016/j.carbon.2005.03.002.
[38] C.J. Kirubakaran, K. Krishnaiah, S.K. Seshadri, Experimental study of the production of activated carbon from coconut shells in a fluidized bed reactor, Ind. Eng. Chem. Res. 30 (1991) 2411–2416. doi:10.1021/ie00059a008.
[39] O. Ioannidou, A. Zabaniotou, Agricultural residues as precursors for activated carbon production—A review, Renew. Sustain. Energy Rev. 11 (2007) 1966–2005. doi:10.1016/j.rser.2006.03.013.
[40] J. Rouquerol, D. Avnir, C.W. Fairbridge, D.H. Everett, J.M. Haynes, N. Pernicone, J.D.F. Ramsay, K.S.W. Sing, K.K. Unger, Recommendations for the characterization of porous solids (Technical Report), Pure Appl. Chem. 66 (2009) 1739–1758. doi:10.1351/pac199466081739.
[41] S. Goriparti, E. Miele, F. De Angelis, E. Di Fabrizio, R. Proietti Zaccaria, C. Capiglia, Review on recent progress of nanostructured anode materials for Li-ion batteries, J. Power Sources. 257 (2014) 421–443. doi:10.1016/j.jpowsour.2013.11.103.
[42] B.D. Zdravkov, J.J. Čermák, M. Šefara, J. Janků, Pore classification in the characterization of porous materials: A perspective, Cent. Eur. J. Chem. 5 (2007) 385–395. doi:10.2478/s11532-007-0017-9.
[43] H. Kurig, M. Russina, I. Tallo, M. Siebenbürger, T. Romann, E. Lust, The suitability of infinite slit-shaped pore model to describe the pores in highly porous carbon materials, Carbon. 100 (2016) 617–624. doi:10.1016/j.carbon.2016.01.061.
[44] L. He, S.M. Chathoth, Y.B. Melnichenko, V. Presser, J. McDonough, Y. Gogotsi, Small-angle neutron scattering characterization of the structure of nanoporous carbons for energy-related applications, Microporous Mesoporous Mater. 149 (2012) 46–54. doi:10.1016/j.micromeso.2011.08.035.
[45] C.J. Jafta, A. Petzold, S. Risse, D. Clemens, D. Wallacher, G. Goerigk, M. Ballauff, Correlating pore size and shape to local disorder in microporous carbon: A combined small angle neutron and X-ray scattering study, Carbon. 123 (2017) 440–447. doi:10.1016/j.carbon.2017.07.046.
[46] S. Mascotto, D. Kuzmicz, D. Wallacher, M. Siebenbürger, D. Clemens, S. Risse, J. Yuan, M. Antonietti, M. Ballauff, Poly(ionic liquid)-derived nanoporous carbon analyzed by combination of gas physisorption and small-angle neutron scattering, Carbon. 82 (2015) 425–435. doi:10.1016/j.carbon.2014.10.086.
[47] A. Jänes, T. Thomberg, H. Kurig, E. Lust, Nanoscale fine-tuning of porosity of carbide-derived carbon prepared from molybdenum carbide, Carbon. 47 (2009) 23–29. doi:10.1016/j.carbon.2008.07.010.

[48] Y. Gogotsi, A. Nikitin, H. Ye, W. Zhou, J.E. Fischer, B. Yi, H.C. Foley, M.W. Barsoum, Nanoporous carbide-derived carbon with tunable pore size, Nat. Mater. 2 (2003) 591. doi:10.1038/nmat957.
[49] I. Tallo, T. Thomberg, H. Kurig, A. Jänes, K. Kontturi, E. Lust, Supercapacitors based on carbide-derived carbons synthesised using HCl and Cl2 as reactants, J. Solid State Electrochem. 17 (2013) 19–28. doi:10.1007/s10008-012-1850-0.
[50] A. Jänes, T. Thomberg, E. Lust, Synthesis and characterisation of nanoporous carbide-derived carbon by chlorination of vanadium carbide, Carbon. 45 (2007) 2717–2722. doi:10.1016/j.carbon.2007.09.041.
[51] S. Welz, M.J. McNallan, Y. Gogotsi, Carbon structures in silicon carbide derived carbon, J. Mater. Process. Technol. 179 (2006) 11–22. doi:10.1016/j.jmatprotec. 2006.03.103.
[52] G.N. Yushin, E.N. Hoffman, A. Nikitin, H. Ye, M.W. Barsoum, Y. Gogotsi, Synthesis of nanoporous carbide-derived carbon by chlorination of titanium silicon carbide, Carbon. 43 (2005) 2075–2082. doi:10.1016/j.carbon.2005.03.014.
[53] S.-H. Yeon, S. Osswald, Y. Gogotsi, J.P. Singer, J.M. Simmons, J.E. Fischer, M.A. Lillo-Ródenas, Á. Linares-Solano, Enhanced methane storage of chemically and physically activated carbide-derived carbon, J. Power Sources. 191 (2009) 560–567. doi:10.1016/j.jpowsour.2009.02.019.
[54] R. Jäger, P.E. Kasatkin, E. Härk, E. Lust, Oxygen reduction on molybdenum carbide derived micromesoporous carbon electrode in alkaline solution, Electrochem. Commun. 35 (2013) 97–99. doi:10.1016/j.elecom.2013.08.001.
[55] R. Dash, J. Chmiola, G. Yushin, Y. Gogotsi, G. Laudisio, J. Singer, J. Fischer, S. Kucheyev, Titanium carbide derived nanoporous carbon for energy-related applications, Carbon. 44 (2006) 2489–2497. doi:10.1016/j.carbon.2006.04.035.
[56] J.D. Buckley, D.D. Edie, Carbon-carbon Materials and Composites, William Andrew, 1993.
[57] O.P. Bahl, R.B. Mathur, K.D. Kundra, Structure of PAN fibres and its relationship to resulting carbon fibre properties, Fibre Sci. Technol. 15 (1981) 147–151. doi:10.1016/0015-0568(81)90067-1.
[58] L. Li Zhang, X. S. Zhao, Carbon-based materials as supercapacitor electrodes, Chem. Soc. Rev. 38 (2009) 2520–2531. doi:10.1039/B813846J.
[59] A.G. Pandolfo, A.F. Hollenkamp, Carbon properties and their role in super-capacitors, J. Power Sources. 157 (2006) 11–27. doi:10.1016/j.jpowsour. 2006.02.065.
[60] D.D. Do, Adsorption Analysis: Equilibria and Kinetics, Imperial College Press, London, 1998.
[61] J. Rouquerol, F. Rouquerol, P. Llewellyn, G. Maurin, K.S.W. Sing, Adsorption by Powders and Porous Solids, Second Edition: Principles, Methodology and Applications, 2 edition, Academic Press, Amsterdam, 2013.
[62] J. Ribeiro-Soares, M.E. Oliveros, C. Garin, M.V. David, L.G.P. Martins, C.A. Almeida, E.H. Martins-Ferreira, K. Takai, T. Enoki, R. Magalhães-Paniago, A. Malachias, A. Jorio, B.S. Archanjo, C.A. Achete, L.G. Cançado, Structural analysis of polycrystalline graphene systems by Raman spectroscopy, Carbon. 95 (2015) 646–652. doi:10.1016/j.carbon.2015.08.020.
[63] F. Tuinstra, J.L. Koenig, Raman Spectrum of Graphite, J. Chem. Phys. 53 (1970) 1126–1130. doi:10.1063/1.1674108.

[64] Y. Wang, D.C. Alsmeyer, R.L. McCreery, Raman spectroscopy of carbon materials: structural basis of observed spectra, Chem. Mater. 2 (1990) 557–563. doi:10.1021/cm00011a018.
[65] T. Ungár, Microstructural parameters from X-ray diffraction peak broadening, Scr. Mater. 51 (2004) 777–781. doi:10.1016/j.scriptamat.2004.05.007.
[66] R. Delhez, T.H. de Keijser, E.J. Mittemeijer, Determination of crystallite size and lattice distortions through X-ray diffraction line profile analysis, Fresenius Z. Für Anal. Chem. 312 (1982) 1–16. doi:10.1007/BF00482725.
[67] J. Filik, P.W. May, S.R.J. Pearce, R.K. Wild, K.R. Hallam, XPS and laser Raman analysis of hydrogenated amorphous carbon films, Diam. Relat. Mater. 12 (2003) 974–978. doi:10.1016/S0925-9635(02)00374-6.
[68] R.J.J. Jansen, H. van Bekkum, XPS of nitrogen-containing functional groups on activated carbon, Carbon. 33 (1995) 1021–1027. doi:10.1016/0008-6223(95)00030-H.
[69] D. Yang, A. Velamakanni, G. Bozoklu, S. Park, M. Stoller, R.D. Piner, S. Stankovich, I. Jung, D.A. Field, C.A. Ventrice, R.S. Ruoff, Chemical analysis of graphene oxide films after heat and chemical treatments by X-ray photoelectron and Micro-Raman spectroscopy, Carbon. 47 (2009) 145–152. doi:10.1016/j.carbon.2008.09.045.
[70] K.S.W. Sing, Reporting physisorption data for gas/solid systems with special reference to the determination of surface area and porosity (Provisional), Pure Appl. Chem. 54 (2009) 2201–2218. doi:10.1351/pac198254112201.
[71] I. Langmuir, The constitution and fundamental properties of solids and liquids. Part I. Solids., J. Am. Chem. Soc. 38 (1916) 2221–2295.
[72] I. Langmuir, The adsorption of gases on plane surfaces of glass, mica and platinum., J. Am. Chem. Soc. 40 (1918) 1361–1403.
[73] S. Brunauer, P.H. Emmett, E. Teller, Adsorption of gases in multimolecular layers, J. Am. Chem. Soc. 60 (1938) 309–319.
[74] J.H. de Boer, B.C. Lippens, B.G. Linsen, J.C.P. Broekhoff, A. van den Heuvel, T.J. Osinga, The *t*-curve of multimolecular N_2-adsorption, J. Colloid Interface Sci. 21 (1966) 405–414. doi:10.1016/0095-8522(66)90006-7.
[75] N.A. Seaton, J.P.R.B. Walton, N. quirke, A new analysis method for the determination of the pore size distribution of porous carbons from nitrogen adsorption measurements, Carbon. 27 (1989) 853–861. doi:10.1016/0008-6223(89)90035-3.
[76] C. Lastoskie, K.E. Gubbins, N. Quirke, Pore size heterogeneity and the carbon slit pore: a density functional theory model, Langmuir. 9 (1993) 2693–2702.
[77] J. Olivier, Wb. Conklin, M. Szombathely, Determination of pore size distribution from density functional theory: a comparison of nitrogen and argon results, Stud. Surf. Sci. Catal. 87 (1994) 81–89.
[78] U.M.B. Marconi, F. Van Swol, Microscopic model for hysteresis and phase equilibria of fluids confined between parallel plates, Phys. Rev. A. 39 (1989) 4109–4116. doi:10.1103/PhysRevA.39.4109.
[79] P.A. Monson, Mean field kinetic theory for a lattice gas model of fluids confined in porous materials, J. Chem. Phys. 128 (2008) 084701. doi:10.1063/1.2837287.
[80] L. Sarkisov, P.A. Monson, Modeling of Adsorption and Desorption in Pores of Simple Geometry Using Molecular Dynamics, Langmuir. 17 (2001) 7600–7604. doi:10.1021/la015521u.
[81] D.W. Siderius, L.D. Gelb, Predicting Gas Adsorption in Complex Microporous and Mesoporous Materials Using a New Density Functional Theory of Finely

Discretized Lattice Fluids, Langmuir. 25 (2009) 1296–1299. doi:10.1021/la803666t.
[82] D.W. Siderius, L.D. Gelb, Extension of the Steele 10-4-3 potential for adsorption calculations in cylindrical, spherical, and other pore geometries, J. Chem. Phys. 135 (2011) 084703. doi:10.1063/1.3626804.
[83] J. Jagiello, J.P. Olivier, 2D-NLDFT adsorption models for carbon slit-shaped pores with surface energetical heterogeneity and geometrical corrugation, Carbon. 55 (2013) 70–80. doi:10.1016/j.carbon.2012.12.011.
[84] J. Jagiello, C. Ania, J.B. Parra, C. Cook, Dual gas analysis of microporous carbons using 2D-NLDFT heterogeneous surface model and combined adsorption data of N_2 and CO_2, Carbon. 91 (2015) 330–337. doi:10.1016/j.carbon.2015.05.004.
[85] W.H. Weber, R. Merlin, Raman scattering in materials science, Springer Science & Business Media, 2013.
[86] A. Kudelski, Analytical applications of Raman spectroscopy, Talanta. 76 (2008) 1–8. doi:10.1016/j.talanta.2008.02.042.
[87] C. Casiraghi, A.C. Ferrari, J. Robertson, Raman spectroscopy of hydrogenated amorphous carbons, Phys. Rev. B. 72 (2005) 085401. doi:10.1103/PhysRevB.72.085401.
[88] J. Schwan, S. Ulrich, V. Batori, H. Ehrhardt, S.R.P. Silva, Raman spectroscopy on amorphous carbon films, J. Appl. Phys. (19960701). doi:10.1063/1.362745.
[89] S. Urbonaite, L. Hälldahl, G. Svensson, Raman spectroscopy studies of carbide derived carbons, Carbon. 46 (2008) 1942–1947.
[90] A.C. Ferrari, Raman spectroscopy of graphene and graphite: Disorder, electron–phonon coupling, doping and nonadiabatic effects, Solid State Commun. 143 (2007) 47–57. doi:10.1016/j.ssc.2007.03.052.
[91] D.W. Turner, M.I.A. Jobory, Determination of Ionization Potentials by Photoelectron Energy Measurement, J. Chem. Phys. 37 (1962) 3007–3008. doi:10.1063/1.1733134.
[92] J.F. Moulder, Handbook of X-ray Photoelectron Spectroscopy: A Reference Book of Standard Spectra for Identification and Interpretation of XPS Data, Physical Electronics, 1995.
[93] H. Stanjek, W. Häusler, Basics of X-ray Diffraction, Hyperfine Interact. 154 (2004) 107–119. doi:10.1023/B:HYPE.0000032028.60546.38.
[94] R.E. Dinnebier, S.J.L. Billinge, Powder Diffraction: Theory and Practice, 2008th ed., Royal Society of Chemistry, Cambridge, 2008.
[95] W.H. Bragg, M. A, F.R. S, W.L. Bragg, B. A, The reflection of X-rays by crystals, Proc R Soc Lond A. 88 (1913) 428–438. doi:10.1098/rspa.1913.0040.
[96] P. Scherrer, Estimation of the size and internal structure of colloidal particles by means of röntgen, Nachr Ges Wiss Gött. 2 (1918) 96–100.
[97] J.S.J. Hargreaves, Some considerations related to the use of the Scherrer equation in powder X-ray diffraction as applied to heterogeneous catalysts, Catal. Struct. React. 2 (2016) 33–37. doi:10.1080/2055074X.2016.1252548.
[98] A.L. Bail, Whole powder pattern decomposition methods and applications: A retrospection, Powder Diffr. 20 (2005) 316–326. doi:10.1154/1.2135315.
[99] P. Thompson, D.E. Cox, J.B. Hastings, Rietveld refinement of Debye–Scherrer synchrotron X-ray data from Al_2O_3, J. Appl. Crystallogr. 20 (1987) 79–83. doi:10.1107/S0021889887087090.
[100] H.I. Becker, Low voltage electrolytic capacitor, US2800616 A, 1957. http://www.google.com/patents/US2800616 (accessed January 2, 2018).

[101] R. Kötz, M. Carlen, Principles and applications of electrochemical capacitors, Electrochimica Acta. 45 (2000) 2483–2498. doi:10.1016/S0013-4686(00)00354-6.
[102] N.-S. Choi, Z. Chen, S.A. Freunberger, X. Ji, Y.-K. Sun, K. Amine, G. Yushin, L.F. Nazar, J. Cho, P.G. Bruce, Challenges Facing Lithium Batteries and Electrical Double-Layer Capacitors, Angew. Chem. Int. Ed. 51 (2012) 9994–10024. doi:10.1002/anie.201201429.
[103] K. Tõnurist, T. Thomberg, A. Jänes, I. Kink, E. Lust, Specific performance of electrical double layer capacitors based on different separator materials in room temperature ionic liquid, Electrochem. Commun. 22 (2012) 77–80. doi:10.1016/j.elecom.2012.05.029.
[104] C. Portet, P.L. Taberna, P. Simon, C. Laberty-Robert, Modification of Al current collector surface by sol–gel deposit for carbon–carbon supercapacitor applications, Electrochimica Acta. 49 (2004) 905–912. doi:10.1016/j.electacta.2003.09.043.
[105] A. Laheäär, P. Przygocki, Q. Abbas, F. Béguin, Appropriate methods for evaluating the efficiency and capacitive behavior of different types of supercapacitors, Electrochem. Commun. 60 (2015) 21–25. doi:10.1016/j.elecom.2015.07.022.
[106] A.B. Fuertes, G. Lota, T.A. Centeno, E. Frackowiak, Templated mesoporous carbons for supercapacitor application, Electrochimica Acta. 50 (2005) 2799–2805. doi:10.1016/j.electacta.2004.11.027.
[107] R. Palm, H. Kurig, K. Tõnurist, A. Jänes, E. Lust, Electrical double layer capacitors based on 1-ethyl-3-methylimidazolium tetrafluoroborate with small addition of acetonitrile, Electrochimica Acta. 85 (2012) 139–144. doi:10.1016/j.electacta.2012.08.030.
[108] R. Palm, H. Kurig, K. Tõnurist, A. Jänes, E. Lust, Influence of Different Organic Solvent Additives on 1-ethyl-3-methylimidazolium Tetrafluoroborate Electrolyte Based Electrical Double Layer Capacitors, J. Electrochem. Soc. 160 (2013) A1741–A1745. doi:10.1149/2.046310jes.
[109] R. Palm, H. Kurig, K. Tõnurist, A. Jänes, E. Lust, Is the mixture of 1-ethyl-3-methylimidazolium tetrafluoroborate and 1-butyl-3-methylimidazolium tetrafluoroborate applicable as electrolyte in electrical double layer capacitors?, Electrochem. Commun. 22 (2012) 203–206. doi:10.1016/j.elecom.2012.06.029.
[110] C. Zhong, Y. Deng, W. Hu, J. Qiao, L. Zhang, J. Zhang, A review of electrolyte materials and compositions for electrochemical supercapacitors, Chem. Soc. Rev. 44 (2015) 7484–7539. doi:10.1039/C5CS00303B.
[111] A. Lewandowski, A. Olejniczak, M. Galinski, I. Stepniak, Performance of carbon–carbon supercapacitors based on organic, aqueous and ionic liquid electrolytes, J. Power Sources. 195 (2010) 5814–5819. doi:10.1016/j.jpowsour.2010.03.082.
[112] K. Fic, G. Lota, M. Meller, E. Frackowiak, Novel insight into neutral medium as electrolyte for high-voltage supercapacitors, Energy Environ. Sci. 5 (2012) 5842–5850. doi:10.1039/C1EE02262H.
[113] L. Demarconnay, E. Raymundo-Piñero, F. Béguin, A symmetric carbon/carbon supercapacitor operating at 1.6V by using a neutral aqueous solution, Electrochem. Commun. 12 (2010) 1275–1278. doi:10.1016/j.elecom.2010.06.036.

[114] M. Armand, F. Endres, D.R. MacFarlane, H. Ohno, B. Scrosati, Ionic-liquid materials for the electrochemical challenges of the future, Nat. Mater. 8 (2009) 621. doi:10.1038/nmat2448.
[115] A.M. O'Mahony, D.S. Silvester, L. Aldous, C. Hardacre, R.G. Compton, Effect of Water on the Electrochemical Window and Potential Limits of Room-Temperature Ionic Liquids, J. Chem. Eng. Data. 53 (2008) 2884–2891. doi:10.1021/je800678e.
[116] H. Oda, A. Yamashita, S. Minoura, M. Okamoto, T. Morimoto, Modification of the oxygen-containing functional group on activated carbon fiber in electrodes of an electric double-layer capacitor, J. Power Sources. 158 (2006) 1510–1516. doi:10.1016/j.jpowsour.2005.10.061.
[117] M. Seredych, D. Hulicova-Jurcakova, G.Q. Lu, T.J. Bandosz, Surface functional groups of carbons and the effects of their chemical character, density and accessibility to ions on electrochemical performance, Carbon. 46 (2008) 1475–1488. doi:10.1016/j.carbon.2008.06.027.
[118] G. Salitra, A. Soffer, L. Eliad, Y. Cohen, D. Aurbach, Carbon Electrodes for Double-Layer Capacitors I. Relations Between Ion and Pore Dimensions, J. Electrochem. Soc. 147 (2000) 2486–2493. doi:10.1149/1.1393557.
[119] A. Jänes, L. Permann, M. Arulepp, E. Lust, Electrochemical characteristics of nanoporous carbide-derived carbon materials in non-aqueous electrolyte solutions, Electrochem. Commun. 6 (2004) 313–318. doi:10.1016/j.elecom. 2004.01.009.
[120] E. Lust, G. Nurk, A. Jänes, M. Arulepp, P. Nigu, P. Möller, S. Kallip, V. Sammelselg, Electrochemical properties of nanoporous carbon electrodes in various nonaqueous electrolytes, J. Solid State Electrochem. 7 (2003) 91–105. doi:10.1007/s10008-002-0316-1.
[121] A.J. Bard, L.R. Faulkner, Electrochemical Methods: Fundamentals and Applications, 2 edition, Wiley, New York, 2000.
[122] E. Barsoukov, J.R. Macdonald, eds., Impedance Spectroscopy: Theory, Experiment, and Applications, 2 edition, Wiley-Interscience, Hoboken, N.J, 2005.
[123] P.L. Taberna, P. Simon, J.F. Fauvarque, Electrochemical Characteristics and Impedance Spectroscopy Studies of Carbon-Carbon Supercapacitors, J. Electrochem. Soc. 150 (2003) A292–A300. doi:10.1149/1.1543948.
[124] E. Lust, A. Jänes, M. Arulepp, Influence of solvent nature on the electrochemical parameters of electrical double layer capacitors, J. Electroanal. Chem. 562 (2004) 33–42. doi:10.1016/j.jelechem.2003.07.034.
[125] C. Solar, A.G. Blanco, A. Vallone, K. Sapag, Adsorption of methane in porous materials as the basis for the storage of natural gas, in: P. Potocnik (Ed.), Nat. Gas, 2010: pp. 205–244. http://cdn.intechopen.com/pdfs/11484.pdf (accessed October 14, 2014).
[126] W. Zhou, H. Wu, M.R. Hartman, T. Yildirim, Hydrogen and Methane Adsorption in Metal−Organic Frameworks: A High-Pressure Volumetric Study, J. Phys. Chem. C. 111 (2007) 16131–16137. doi:10.1021/jp074889i.
[127] K. Seki, Design of an adsorbent with an ideal pore structure for methane adsorption using metal complexes, Chem. Commun. 0 (2001) 1496–1497. doi:10.1039/B104204C.
[128] S. Cavenati, C.A. Grande, A.E. Rodrigues, Adsorption Equilibrium of Methane, Carbon Dioxide, and Nitrogen on Zeolite 13X at High Pressures, J. Chem. Eng. Data. 49 (2004) 1095–1101. doi:10.1021/je0498917.

[129] M.M.K. Salem, P. Braeuer, M. v. Szombathely, M. Heuchel, P. Harting, K. Quitzsch, M. Jaroniec, Thermodynamics of High-Pressure Adsorption of Argon, Nitrogen, and Methane on Microporous Adsorbents, Langmuir. 14 (1998) 3376–3389. doi:10.1021/la970119u.
[130] D.-Y. Peng, D.B. Robinson, A new two-constant equation of state, Ind. Eng. Chem. Fundam. 15 (1976) 59–64.
[131] J.D. Van der Waals, F. Roth, The continuity of the liquid and gaseous states, 1873.
[132] O. Redlich, J.N. Kwong, On the thermodynamics of solutions. V. An equation of state. Fugacities of gaseous solutions., Chem. Rev. 44 (1949) 233–244.
[133] G. Soave, Equilibrium constants from a modified Redlich-Kwong equation of state, Chem. Eng. Sci. 27 (1972) 1197–1203.
[134] Y. Zhou, L. Zhou, Fundamentals of High Pressure Adsorption, Langmuir. 25 (2009) 13461–13466. doi:10.1021/la901956g.
[135] R. Sips, Combined form of Langmuir and Freundlich equations, J Chem Phys. 16 (1948) 490–495.
[136] J. Toth, State equation of the solid-gas interface layers, Acta Chim Hung. 69 (1971) 311–328.
[137] M. Temkin, V. Pyzhev, Kinetics of ammonia synthesis on promoted iron catalysts, Acta Physiochim URSS. 12 (1940) 217–222.
[138] J.H. Van't Hoff, Etudes de dynamique chimique, Muller, 1884.
[139] R.A. Varin, T. Czujko, Z.S. Wronski, Nanomaterials for Solid State Hydrogen Storage, Springer Science & Business Media, 2009.
[140] K.M. Thomas, Hydrogen adsorption and storage on porous materials, Catal. Today. 120 (2007) 389–398. doi:10.1016/j.cattod.2006.09.015.
[141] X. Shao, W. Wang, R. Xue, Z. Shen, Adsorption of Methane and Hydrogen on Mesocarbon Microbeads by Experiment and Molecular Simulation, J. Phys. Chem. B. 108 (2004) 2970–2978. doi:10.1021/jp035715d.
[142] M. Hirscher, Handbook of Hydrogen Storage: New Materials for Future Energy Storage, John Wiley & Sons, 2010.
[143] T. Graham, XXII.—On the absorption and dialytic separation of gases by colloid septa, J. Chem. Soc. 20 (1867) 235–288.
[144] J. Wang, A.D. Ebner, J.A. Ritter, On the Reversibility of Hydrogen Storage in Novel Complex Hydrides, Adsorption. 11 (2005) 811–816. doi:10.1007/s10450-005-6028-y.
[145] H. Vikström, S. Davidsson, M. Höök, Lithium availability and future production outlooks, Appl. Energy. 110 (2013) 252–266. doi:10.1016/j.apenergy.2013.04.005.
[146] J. Dilts, E. Ashby, Thermal decomposition of complex metal hydrides, Inorg. Chem. 11 (1972) 1230–1236.
[147] S. Singh, S.W.H. Eijt, J. Huot, W.A. Kockelmann, M. Wagemaker, F.M. Mulder, The $TiCl_3$ catalyst in $NaAlH_4$ for hydrogen storage induces grain refinement and impacts on hydrogen vacancy formation, Acta Mater. 55 (2007) 5549–5557. doi:10.1016/j.actamat.2007.06.028.
[148] A. Zaluska, L. Zaluski, J.O. Ström-Olsen, Sodium alanates for reversible hydrogen storage, J. Alloys Compd. 298 (2000) 125–134. doi:10.1016/S0925-8388(99)00666-0.
[149] G. Streukens, B. Bogdanović, M. Felderhoff, F. Schüth, Dependence of dissociation pressure upon doping level of Ti-doped sodium alanate – a possibility

for “thermodynamic tailoring” of the system, Phys. Chem. Chem. Phys. 8 (2006) 2889–2892. doi:10.1039/B603268K.
[150] G. Sandrock, K. Gross, G. Thomas, Effect of Ti-catalyst content on the reversible hydrogen storage properties of the sodium alanates, J. Alloys Compd. 339 (2002) 299–308. doi:10.1016/S0925-8388(01)02014-X.
[151] C.P. Baldé, B.P.C. Hereijgers, J.H. Bitter, K.P. de Jong, Sodium Alanate Nanoparticles − Linking Size to Hydrogen Storage Properties, J. Am. Chem. Soc. 130 (2008) 6761–6765. doi:10.1021/ja710667v.
[152] J. Gao, P. Adelhelm, M.H.W. Verkuijlen, C. Rongeat, M. Herrich, P.J.M. van Bentum, O. Gutfleisch, A.P.M. Kentgens, K.P. de Jong, P.E. de Jongh, Confinement of NaAlH4 in Nanoporous Carbon: Impact on H_2 Release, Reversibility, and Thermodynamics, J. Phys. Chem. C. 114 (2010) 4675–4682. doi:10.1021/jp910511g.
[153] T.K. Nielsen, M. Polanski, D. Zasada, P. Javadian, F. Besenbacher, J. Bystrzycki, J. Skibsted, T.R. Jensen, Improved Hydrogen Storage Kinetics of Nanoconfined NaAlH4 Catalyzed with TiCl3 Nanoparticles, ACS Nano. 5 (2011) 4056–4064. doi:10.1021/nn200643b.
[154] J. Jagiello, Stable numerical solution of the adsorption integral equation using splines, Langmuir. 10 (1994) 2778–2785.
[155] M.P. Seah, I.S. Gilmore, S.J. Spencer, Quantitative XPS: I. Analysis of X-ray photoelectron intensities from elemental data in a digital photoelectron database, J. Electron Spectrosc. Relat. Phenom. 120 (2001) 93–111. doi:10.1016/S0368-2048(01)00311-5.
[156] F.O. Mertens, Determination of absolute adsorption in highly ordered porous media, Surf. Sci. 603 (2009) 1979–1984. doi:10.1016/j.susc.2008.10.054.
[157] H. Wang, M. Yoshio, Effect of cation on the performance of AC/graphite capacitor, Electrochem. Commun. 10 (2008) 382–386. doi:10.1016/j.elecom.2007.12.027.
[158] A. Jänes, H. Kurig, T. Romann, E. Lust, Novel doubly charged cation based electrolytes for non-aqueous supercapacitors, Electrochem. Commun. 12 (2010) 535–539. doi:10.1016/j.elecom.2010.01.037.
[159] C. Portet, P.L. Taberna, P. Simon, E. Flahaut, C. Laberty-Robert, High power density electrodes for Carbon supercapacitor applications, Electrochimica Acta. 50 (2005) 4174–4181. doi:10.1016/j.electacta.2005.01.038.
[160] E. Lust, A. Jänes, T. Pärn, P. Nigu, Influence of nanoporous carbon electrode thickness on the electrochemical characteristics of a nanoporous carbon|tetraethylammonium tetrafluoroborate in acetonitrile solution interface, J. Solid State Electrochem. 8 (2004) 224–237. doi:10.1007/s10008-003-0396-6.
[161] D. Pech, M. Brunet, H. Durou, P. Huang, V. Mochalin, Y. Gogotsi, P.-L. Taberna, P. Simon, Ultrahigh-power micrometre-sized supercapacitors based on onion-like carbon, Nat. Nanotechnol. 5 (2010) 651–654. doi:10.1038/nnano.2010.162.
[162] F. Endres, D.R. MacFarlane, A. Abbott, Electrodeposition from Ionic Liquids, John Wiley & Sons, 2008.
[163] P. Llewellyn, F. Rodriquez-Reinoso, J. Rouqerol, N. Seaton, Is the BET equation applicable to microporous adsorbents?, Stud. Surf. Sci. Catal. 160 (2007) 49.

10. SUMMARY IN ESTONIAN

Süsinikmaterjalid energiasalvestus rakendustes

Süsinikmaterjalide omaduste mõju energiasalvestus rakendustele uuriti kasutades mitmeid suure eripinnaga mikropoorseid süsinikmaterjale. Süsinikmaterjale kasutati elektroodmaterjalina elektrilise kaksikkihi kondensaatorites laengu salvestamiseks, adsorbentidena metaani salvestamiseks ning kandematerjalina kompleksmetallhüdriidi sidumiseks pinnale ja pooridesse, selleks et pöörduvalt vesinikku salvestada. Uuritavateks süsinikmaterjali karakteristikuteks olid eripindala, salvestatud energia hulk pinnaühiku kohta, poori suurus, poori suurusjaotus ning struktuurne korrapära (keskmine korrelatsiooni pikkus). Süsinikmaterjalide eripindala, poori ruumala ning poorijaotus määrati N_2 ja CO_2 adsorptsiooni meetoditega. Süsinikmaterjalide keskmine korrelatsiooni pikkus määrati Raman spektrist.

Elektrokeemilised mõõtmised teostati kolmel süsinikkangal ning ühel karbiidset päritolu süsinikul (KPS) põhineval elektroodmaterjalil. Elektrolüüdina kasutati 1 M trietüülmetüülammonium tetrafluoroboraati ($TEMABF_4$) atsetonitriilis (AN) ning ioonset vedelikku 1-etüül-3-metüülimidasoolium tetrafluoroboraati ($EMImBF_4$). Määrati elektroodide paksused ning elektroodmaterjalid kaeti ühelt poolt Al kihiga juhtivuse parandamiseks. Antud töös toodi välja liiga väikeste pooride sobimatus elektrilise kaksikkihi moodustamiseks, elektroodi paksuse mõju võimsustihedusele ja eripindala suurendamise väike mõju energiatihedusele, juhul kui eripindala on suurem kui > 500 m^2 g^{-1}. Näidati eripindala suuremat mõju energiatihedusele ioonse vedeliku, $EMImBF_4$, põhise elektrolüüdi kasutamisel, võrreldes 1 M $TEMABF_4$ AN elektrolüüdiga.

Metaani adsorptiooni uuriti kolmel KPS-l, mis olid erineva ja selgelt määratletud poori suurusjaotusega ja keskmise korrelatsiooni pikkusega. Metaani adsorptsiooni liig mõõdeti metaani osarõhkude vahemikus 0.03 kuni 1.35 MPa ning temperatuurivahemikus -100 kuni 40 °C. Summaarne adsorbeerunud metaani hulk arvutati metaani adsorptsiooni liiast kasutades muudetud Langmuiri isotermi võrrandit. Metaani adsorptsiooni entalpiad ja entroopiad arvutati adsorbeerunud metaani isotermidest Van't Hoffi võrrandit kasutades. Eripinnaga normeeritud maksimaalselt adsorbeerunud metaani hulgad olid peaaegu võrdsed kõikide uuritud KPS-e puhul. Seega maksimaalne metaani hulk, mida saab adsorbeerida ei sõltunud poori suurusest, ega süsinikmaterjali korrapärast uuritud KPS-e puhul. Adsorptsioonitasakaalus on adsorptsioon eelistatud süsinikmaterjalide puhul mis on korrapäratumad ning väiksemate pooridega.

Suure eripinnaga mikropoorset süsinikku, RP-20, kasutati kandematerjalina kompleksmetallhüdriidi, $NaAlH_4$, sidumiseks. 10 kuni 60 mass% $NaAlH_4$-i kanti RP-20 pinnale ja pooridesse lahusega immutamise meetodil. Eraldunud vesiniku hulk määrati ühtlase kiirusega temperatuuri tõstes. $NaAlH_4$ ja tema laguproduktide kristalliitide olemasolu ning suurused määrati röntgendifraktsiooni meetodiga. Vesiniku eraldumise temperatuuri vähendati 170 °C-lt 40 °C-ni $NaAlH_4$-ja sidumisega RP-20-e pooridesse ja pinnale. Rakendati 10 vesiniku

eraldamise ja täislaadimise tsüklit $NaAlH_4$/RP-20 komposiitmaterjalidele ja puhtale $NaAlH_4$-le. 60 mass% $NaAlH_4$-ga komposiitmaterjali vesiniku eraldumise temperatuur alanes ning kristalne $NaAlH_4$ faas kadus tsükleerimise käigus. $NaAlH_4$ sidumine mikropoorse süsinikmaterjali pinnale ja pooridesse põhjustas tsükleerimise käigus $NaAlH_4$ ümberorganiseerumise väiksemateks või amorfseteks osakesteks.

11. ACKNOWLEDGEMENTS

I am most grateful to my supervisors, Ph.D. Heisi Kurig and Prof. Enn Lust, for unceasing support towards me and my work, without them this work wouldn't have been possible. I am thankful to Jaan Aruväli for the measurements and consultations in regard to X-ray diffraction, to Tavo Romann for the measurements of Raman spectra and the deposition of Al on the electrode materials, to Urmas Joost for the X-ray photoelectron spectroscopy measurements, to Indrek Tallo and Thomas Thomberg for the synthesis of carbide-derived carbons, to Ronald Väli for the expertise in regard to preparing electrode materials and to Alar Jänes for expertise.

I am very thankful for the unending support from family and friends towards my efforts in the field of science.

The research was financially supported by the EU through the European Regional Development Fund (Centres of Excellence 2014-2020.4.01.15-0011 and 3.2.0101-0030); Estonian Research Council (Institutional Research Grant. IUT20-13 and Personal Research Grant PUT55); Estonian national transmission system operator Elering (scholarship 1.1-4/2016/420); and by Graduate School "Functional Materials and Technologies" funded by the European Regional Development Fund (project 2014-2020.4.01.16-0027).

12. PUBLICATIONS

CURRICULUM VITAE

Name: Rasmus Palm
Date of Birth: June 28, 1989
Citizenship: Estonian
Address: Ropka 10–12, 50111 Tartu, Estonia
Telephone: +372 5664 5152
E-mail: rasmus.palm@ut.ee

Education:

2014–	University of Tartu, PhD student, Chemistry
2012–2014	University of Tartu, MSc, Material Sciences
2009–2012	University of Tartu, BSc, Chemistry

Professional career:

03.2011–	University of Tartu Chemist in the Chair of Applied Electrochemistry

List of publications:

1. R. Palm, H. Kurig, J. Aruväli, E. Lust, Microporous and Mesoporous Mater. 264 (2018) 8
2. R.Palm, H. Kurig, T. Romann, U. Joost, R. Kanarbik, R. Väli, I. Tallo, T. Thomberg, A. Jänes, E. Lust, J. Electrochem. Soc. 164(2) (2017) A453
3. R. Palm, I. Tallo, T. Romann, H. Kurig, Microporous and Mesoporous Mater. 218 (2015) 167
4. R. Palm, H. Kurig, K. Tõnurist, A Jänes, E. Lust, J. Electrochem. Soc. 160(10) (2013) A1741
5. R. Palm, H. Kurig, K. Tõnurist, A. Jänes, E. Lust, Electrochem. Commun. 22 (2012) 203
6. R. Palm, H. Kurig, K. Tõnurist, A. Jänes, E. Lust, Electrochim. Acta 85 (2012) 139
7. E. Lust, L. Siinor, H. Kurig, T. Romann, V. Ivaništšev, C. Siimenson, T. Thomberg, J. Kruusma, K. Lust, P. Pikma, E. Anderson, V. Grozovski, R. Palm, L. Läll, A. Ruzanov, T. Tooming, O. Oll, A. Jänes, ECS Transaction 75(15) (2016) 161
8. T. Thomber, T. Tooming, R. Tavo, R. Palm, A. Jänes, E. Lust, ECS Trans. 58(27) (2014) 3

ELULOOKIRJELDUS

Nimi: Rasmus Palm
Sünniaeg: 28. juuni 1989
Kodakontsus: Eesti
Aadress: Ropka 10–12, 50111 Tartu, Eesti
Telefon: +372 5664 5152
E-post: rasmus.palm@ut.ee

Haridus:

2014–	Tartu Ülikool, Doktorant, Keemia eriala
2012–2014	Tartu Ülikool, MSc, Materjaliteaduse eriala
2009–2012	Tartu Ülikool, BSc., Keemia eriala

Teenistuskäik:

03.2011–	Tartu Ülikool Keemik Rakendusliku Elektrokeemia õppetoolis

Teaduspublikatsioonide loetelu:

1. R. Palm, H. Kurig, J. Aruväli, E. Lust, Microporous and Mesoporous Mater. 264 (2018) 8
2. R.Palm, H. Kurig, T. Romann, U. Joost, R. Kanarbik, R. Väli, I. Tallo, T. Thomberg, A. Jänes, E. Lust, J. Electrochem. Soc. 164(2) (2017) A453
3. R. Palm, I. Tallo, T. Romann, H. Kurig, Microporous and Mesoporous Mater. 218 (2015) 167
4. R. Palm, H. Kurig, K. Tõnurist, A Jänes, E. Lust, J. Electrochem. Soc. 160(10) (2013) A1741
5. R. Palm, H. Kurig, K. Tõnurist, A. Jänes, E. Lust, Electrochem. Commun. 22 (2012) 203
6. R. Palm, H. Kurig, K. Tõnurist, A. Jänes, E. Lust, Electrochim. Acta 85 (2012) 139
7. E. Lust, L. Siinor, H. Kurig, T. Romann, V. Ivaništšev, C. Siimenson, T. Thomberg, J. Kruusma, K. Lust, P. Pikma, E. Anderson, V. Grozovski, R. Palm, L. Läll, A. Ruzanov, T. Tooming, O. Oll, A. Jänes, ECS Transaction 75(15) (2016) 161
8. T. Thomber, T. Tooming, R. Tavo, R. Palm, A. Jänes, E. Lust, ECS Trans. 58(27) (2014) 3

DISSERTATIONES CHIMICAE UNIVERSITATIS TARTUENSIS

1. **Toomas Tamm.** Quantum-chemical simulation of solvent effects. Tartu, 1993, 110 p.
2. **Peeter Burk.** Theoretical study of gas-phase acid-base equilibria. Tartu, 1994, 96 p.
3. **Victor Lobanov.** Quantitative structure-property relationships in large descriptor spaces. Tartu, 1995, 135 p.
4. **Vahur Mäemets.** The ^{17}O and ^{1}H nuclear magnetic resonance study of H_2O in individual solvents and its charged clusters in aqueous solutions of electrolytes. Tartu, 1997, 140 p.
5. **Andrus Metsala.** Microcanonical rate constant in nonequilibrium distribution of vibrational energy and in restricted intramolecular vibrational energy redistribution on the basis of slater's theory of unimolecular reactions. Tartu, 1997, 150 p.
6. **Uko Maran.** Quantum-mechanical study of potential energy surfaces in different environments. Tartu, 1997, 137 p.
7. **Alar Jänes.** Adsorption of organic compounds on antimony, bismuth and cadmium electrodes. Tartu, 1998, 219 p.
8. **Kaido Tammeveski.** Oxygen electroreduction on thin platinum films and the electrochemical detection of superoxide anion. Tartu, 1998, 139 p.
9. **Ivo Leito.** Studies of Brønsted acid-base equilibria in water and non-aqueous media. Tartu, 1998, 101 p.
10. **Jaan Leis.** Conformational dynamics and equilibria in amides. Tartu, 1998, 131 p.
11. **Toonika Rinken.** The modelling of amperometric biosensors based on oxidoreductases. Tartu, 2000, 108 p.
12. **Dmitri Panov.** Partially solvated Grignard reagents. Tartu, 2000, 64 p.
13. **Kaja Orupõld.** Treatment and analysis of phenolic wastewater with microorganisms. Tartu, 2000, 123 p.
14. **Jüri Ivask.** Ion Chromatographic determination of major anions and cations in polar ice core. Tartu, 2000, 85 p.
15. **Lauri Vares.** Stereoselective Synthesis of Tetrahydrofuran and Tetrahydropyran Derivatives by Use of Asymmetric Horner-Wadsworth-Emmons and Ring Closure Reactions. Tartu, 2000, 184 p.
16. **Martin Lepiku.** Kinetic aspects of dopamine D_2 receptor interactions with specific ligands. Tartu, 2000, 81 p.
17. **Katrin Sak.** Some aspects of ligand specificity of P2Y receptors. Tartu, 2000, 106 p.
18. **Vello Pällin.** The role of solvation in the formation of iotsitch complexes. Tartu, 2001, 95 p.
19. **Katrin Kollist.** Interactions between polycyclic aromatic compounds and humic substances. Tartu, 2001, 93 p.

20. **Ivar Koppel.** Quantum chemical study of acidity of strong and superstrong Brønsted acids. Tartu, 2001, 104 p.
21. **Viljar Pihl.** The study of the substituent and solvent effects on the acidity of OH and CH acids. Tartu, 2001, 132 p.
22. **Natalia Palm.** Specification of the minimum, sufficient and significant set of descriptors for general description of solvent effects. Tartu, 2001, 134 p.
23. **Sulev Sild.** QSPR/QSAR approaches for complex molecular systems. Tartu, 2001, 134 p.
24. **Ruslan Petrukhin.** Industrial applications of the quantitative structure-property relationships. Tartu, 2001, 162 p.
25. **Boris V. Rogovoy.** Synthesis of (benzotriazolyl)carboximidamides and their application in relations with *N*- and *S*-nucleophyles. Tartu, 2002, 84 p.
26. **Koit Herodes.** Solvent effects on UV-vis absorption spectra of some solvatochromic substances in binary solvent mixtures: the preferential solvation model. Tartu, 2002, 102 p.
27. **Anti Perkson.** Synthesis and characterisation of nanostructured carbon. Tartu, 2002, 152 p.
28. **Ivari Kaljurand.** Self-consistent acidity scales of neutral and cationic Brønsted acids in acetonitrile and tetrahydrofuran. Tartu, 2003, 108 p.
29. **Karmen Lust.** Adsorption of anions on bismuth single crystal electrodes. Tartu, 2003, 128 p.
30. **Mare Piirsalu.** Substituent, temperature and solvent effects on the alkaline hydrolysis of substituted phenyl and alkyl esters of benzoic acid. Tartu, 2003, 156 p.
31. **Meeri Sassian.** Reactions of partially solvated Grignard reagents. Tartu, 2003, 78 p.
32. **Tarmo Tamm.** Quantum chemical modelling of polypyrrole. Tartu, 2003. 100 p.
33. **Erik Teinemaa.** The environmental fate of the particulate matter and organic pollutants from an oil shale power plant. Tartu, 2003. 102 p.
34. **Jaana Tammiku-Taul.** Quantum chemical study of the properties of Grignard reagents. Tartu, 2003. 120 p.
35. **Andre Lomaka.** Biomedical applications of predictive computational chemistry. Tartu, 2003. 132 p.
36. **Kostyantyn Kirichenko.** Benzotriazole – Mediated Carbon–Carbon Bond Formation. Tartu, 2003. 132 p.
37. **Gunnar Nurk.** Adsorption kinetics of some organic compounds on bismuth single crystal electrodes. Tartu, 2003, 170 p.
38. **Mati Arulepp.** Electrochemical characteristics of porous carbon materials and electrical double layer capacitors. Tartu, 2003, 196 p.
39. **Dan Cornel Fara.** QSPR modeling of complexation and distribution of organic compounds. Tartu, 2004, 126 p.
40. **Riina Mahlapuu.** Signalling of galanin and amyloid precursor protein through adenylate cyclase. Tartu, 2004, 124 p.

41. **Mihkel Kerikmäe.** Some luminescent materials for dosimetric applications and physical research. Tartu, 2004, 143 p.
42. **Jaanus Kruusma.** Determination of some important trace metal ions in human blood. Tartu, 2004, 115 p.
43. **Urmas Johanson.** Investigations of the electrochemical properties of polypyrrole modified electrodes. Tartu, 2004, 91 p.
44. **Kaido Sillar.** Computational study of the acid sites in zeolite ZSM-5. Tartu, 2004, 80 p.
45. **Aldo Oras.** Kinetic aspects of dATPαS interaction with $P2Y_1$ receptor. Tartu, 2004, 75 p.
46. **Erik Mölder.** Measurement of the oxygen mass transfer through the air-water interface. Tartu, 2005, 73 p.
47. **Thomas Thomberg.** The kinetics of electroreduction of peroxodisulfate anion on cadmium (0001) single crystal electrode. Tartu, 2005, 95 p.
48. **Olavi Loog.** Aspects of condensations of carbonyl compounds and their imine analogues. Tartu, 2005, 83 p.
49. **Siim Salmar.** Effect of ultrasound on ester hydrolysis in aqueous ethanol. Tartu, 2006, 73 p.
50. **Ain Uustare.** Modulation of signal transduction of heptahelical receptors by other receptors and G proteins. Tartu, 2006, 121 p.
51. **Sergei Yurchenko.** Determination of some carcinogenic contaminants in food. Tartu, 2006, 143 p.
52. **Kaido Tämm.** QSPR modeling of some properties of organic compounds. Tartu, 2006, 67 p.
53. **Olga Tšubrik.** New methods in the synthesis of multisubstituted hydrazines. Tartu. 2006, 183 p.
54. **Lilli Sooväli.** Spectrophotometric measurements and their uncertainty in chemical analysis and dissociation constant measurements. Tartu, 2006, 125 p.
55. **Eve Koort.** Uncertainty estimation of potentiometrically measured ph and pK_a values. Tartu, 2006, 139 p.
56. **Sergei Kopanchuk.** Regulation of ligand binding to melanocortin receptor subtypes. Tartu, 2006, 119 p.
57. **Silvar Kallip.** Surface structure of some bismuth and antimony single crystal electrodes. Tartu, 2006, 107 p.
58. **Kristjan Saal.** Surface silanization and its application in biomolecule coupling. Tartu, 2006, 77 p.
59. **Tanel Tätte.** High viscosity $Sn(OBu)_4$ oligomeric concentrates and their applications in technology. Tartu, 2006, 91 p.
60. **Dimitar Atanasov Dobchev**. Robust QSAR methods for the prediction of properties from molecular structure. Tartu, 2006, 118 p.
61. **Hannes Hagu**. Impact of ultrasound on hydrophobic interactions in solutions. Tartu, 2007, 81 p.
62. **Rutha Jäger.** Electroreduction of peroxodisulfate anion on bismuth electrodes. Tartu, 2007, 142 p.

63. **Kaido Viht.** Immobilizable bisubstrate-analogue inhibitors of basophilic protein kinases: development and application in biosensors. Tartu, 2007, 88 p.
64. **Eva-Ingrid Rõõm.** Acid-base equilibria in nonpolar media. Tartu, 2007, 156 p.
65. **Sven Tamp.** DFT study of the cesium cation containing complexes relevant to the cesium cation binding by the humic acids. Tartu, 2007, 102 p.
66. **Jaak Nerut.** Electroreduction of hexacyanoferrate(III) anion on Cadmium (0001) single crystal electrode. Tartu, 2007, 180 p.
67. **Lauri Jalukse.** Measurement uncertainty estimation in amperometric dissolved oxygen concentration measurement. Tartu, 2007, 112 p.
68. **Aime Lust.** Charge state of dopants and ordered clusters formation in CaF_2:Mn and CaF_2:Eu luminophors. Tartu, 2007, 100 p.
69. **Iiris Kahn**. Quantitative Structure-Activity Relationships of environmentally relevant properties. Tartu, 2007, 98 p.
70. **Mari Reinik.** Nitrates, nitrites, N-nitrosamines and polycyclic aromatic hydrocarbons in food: analytical methods, occurrence and dietary intake. Tartu, 2007, 172 p.
71. **Heili Kasuk.** Thermodynamic parameters and adsorption kinetics of organic compounds forming the compact adsorption layer at Bi single crystal electrodes. Tartu, 2007, 212 p.
72. **Erki Enkvist.** Synthesis of adenosine-peptide conjugates for biological applications. Tartu, 2007, 114 p.
73. **Svetoslav Hristov Slavov**. Biomedical applications of the QSAR approach. Tartu, 2007, 146 p.
74. **Eneli Härk.** Electroreduction of complex cations on electrochemically polished Bi(*hkl*) single crystal electrodes. Tartu, 2008, 158 p.
75. **Priit Möller.** Electrochemical characteristics of some cathodes for medium temperature solid oxide fuel cells, synthesized by solid state reaction technique. Tartu, 2008, 90 p.
76. **Signe Viggor.** Impact of biochemical parameters of genetically different pseudomonads at the degradation of phenolic compounds. Tartu, 2008, 122 p.
77. **Ave Sarapuu.** Electrochemical reduction of oxygen on quinone-modified carbon electrodes and on thin films of platinum and gold. Tartu, 2008, 134 p.
78. **Agnes Kütt.** Studies of acid-base equilibria in non-aqueous media. Tartu, 2008, 198 p.
79. **Rouvim Kadis.** Evaluation of measurement uncertainty in analytical chemistry: related concepts and some points of misinterpretation. Tartu, 2008, 118 p.
80. **Valter Reedo.** Elaboration of IVB group metal oxide structures and their possible applications. Tartu, 2008, 98 p.
81. **Aleksei Kuznetsov.** Allosteric effects in reactions catalyzed by the cAMP-dependent protein kinase catalytic subunit. Tartu, 2009, 133 p.

82. **Aleksei Bredihhin.** Use of mono- and polyanions in the synthesis of multisubstituted hydrazine derivatives. Tartu, 2009, 105 p.
83. **Anu Ploom.** Quantitative structure-reactivity analysis in organosilicon chemistry. Tartu, 2009, 99 p.
84. **Argo Vonk.** Determination of adenosine A_{2A}- and dopamine D_1 receptor-specific modulation of adenylate cyclase activity in rat striatum. Tartu, 2009, 129 p.
85. **Indrek Kivi.** Synthesis and electrochemical characterization of porous cathode materials for intermediate temperature solid oxide fuel cells. Tartu, 2009, 177 p.
86. **Jaanus Eskusson.** Synthesis and characterisation of diamond-like carbon thin films prepared by pulsed laser deposition method. Tartu, 2009, 117 p.
87. **Marko Lätt.** Carbide derived microporous carbon and electrical double layer capacitors. Tartu, 2009, 107 p.
88. **Vladimir Stepanov.** Slow conformational changes in dopamine transporter interaction with its ligands. Tartu, 2009, 103 p.
89. **Aleksander Trummal.** Computational Study of Structural and Solvent Effects on Acidities of Some Brønsted Acids. Tartu, 2009, 103 p.
90. **Eerold Vellemäe.** Applications of mischmetal in organic synthesis. Tartu, 2009, 93 p.
91. **Sven Parkel.** Ligand binding to 5-HT_{1A} receptors and its regulation by Mg^{2+} and Mn^{2+}. Tartu, 2010, 99 p.
92. **Signe Vahur.** Expanding the possibilities of ATR-FT-IR spectroscopy in determination of inorganic pigments. Tartu, 2010, 184 p.
93. **Tavo Romann**. Preparation and surface modification of bismuth thin film, porous, and microelectrodes. Tartu, 2010, 155 p.
94. **Nadežda Aleksejeva.** Electrocatalytic reduction of oxygen on carbon nanotube-based nanocomposite materials. Tartu, 2010, 147 p.
95. **Marko Kullapere.** Electrochemical properties of glassy carbon, nickel and gold electrodes modified with aryl groups. Tartu, 2010, 233 p.
96. **Liis Siinor.** Adsorption kinetics of ions at Bi single crystal planes from aqueous electrolyte solutions and room-temperature ionic liquids. Tartu, 2010, 101 p.
97. **Angela Vaasa.** Development of fluorescence-based kinetic and binding assays for characterization of protein kinases and their inhibitors. Tartu 2010, 101 p.
98. **Indrek Tulp.** Multivariate analysis of chemical and biological properties. Tartu 2010, 105 p.
99. **Aare Selberg.** Evaluation of environmental quality in Northern Estonia by the analysis of leachate. Tartu 2010, 117 p.
100. **Darja Lavõgina.** Development of protein kinase inhibitors based on adenosine analogue-oligoarginine conjugates. Tartu 2010, 248 p.
101. **Laura Herm.** Biochemistry of dopamine D_2 receptors and its association with motivated behaviour. Tartu 2010, 156 p.

102. **Terje Raudsepp.** Influence of dopant anions on the electrochemical properties of polypyrrole films. Tartu 2010, 112 p.
103. **Margus Marandi.** Electroformation of Polypyrrole Films: *In-situ* AFM and STM Study. Tartu 2011, 116 p.
104. **Kairi Kivirand.** Diamine oxidase-based biosensors: construction and working principles. Tartu, 2011, 140 p.
105. **Anneli Kruve.** Matrix effects in liquid-chromatography electrospray mass-spectrometry. Tartu, 2011, 156 p.
106. **Gary Urb.** Assessment of environmental impact of oil shale fly ash from PF and CFB combustion. Tartu, 2011, 108 p.
107. **Nikita Oskolkov.** A novel strategy for peptide-mediated cellular delivery and induction of endosomal escape. Tartu, 2011, 106 p.
108. **Dana Martin.** The QSPR/QSAR approach for the prediction of properties of fullerene derivatives. Tartu, 2011, 98 p.
109. **Säde Viirlaid.** Novel glutathione analogues and their antioxidant activity. Tartu, 2011, 106 p.
110. **Ülis Sõukand.** Simultaneous adsorption of Cd^{2+}, Ni^{2+}, and Pb^{2+} on peat. Tartu, 2011, 124 p.
111. **Lauri Lipping.** The acidity of strong and superstrong Brønsted acids, an outreach for the "limits of growth": a quantum chemical study. Tartu, 2011, 124 p.
112. **Heisi Kurig.** Electrical double-layer capacitors based on ionic liquids as electrolytes. Tartu, 2011, 146 p.
113. **Marje Kasari.** Bisubstrate luminescent probes, optical sensors and affinity adsorbents for measurement of active protein kinases in biological samples. Tartu, 2012, 126 p.
114. **Kalev Takkis.** Virtual screening of chemical databases for bioactive molecules. Tartu, 2012, 122 p.
115. **Ksenija Kisseljova**. Synthesis of aza-β^3-amino acid containing peptides and kinetic study of their phosphorylation by protein kinase A. Tartu, 2012, 104 p.
116. **Riin Rebane.** Advanced method development strategy for derivatization LC/ESI/MS. Tartu, 2012, 184 p.
117. **Vladislav Ivaništšev.** Double layer structure and adsorption kinetics of ions at metal electrodes in room temperature ionic liquids. Tartu, 2012, 128 p.
118. **Irja Helm.** High accuracy gravimetric Winkler method for determination of dissolved oxygen. Tartu, 2012, 139 p.
119. **Karin Kipper.** Fluoroalcohols as Components of LC-ESI-MS Eluents: Usage and Applications. Tartu, 2012, 164 p.
120. **Arno Ratas.** Energy storage and transfer in dosimetric luminescent materials. Tartu, 2012, 163 p.
121. **Reet Reinart-Okugbeni**. Assay systems for characterisation of subtype-selective binding and functional activity of ligands on dopamine receptors. Tartu, 2012, 159 p.

122. **Lauri Sikk.** Computational study of the Sonogashira cross-coupling reaction. Tartu, 2012, 81 p.
123. **Karita Raudkivi.** Neurochemical studies on inter-individual differences in affect-related behaviour of the laboratory rat. Tartu, 2012, 161 p.
124. **Indrek Saar.** Design of GalR2 subtype specific ligands: their role in depression-like behavior and feeding regulation. Tartu, 2013, 126 p.
125. **Ann Laheäär.** Electrochemical characterization of alkali metal salt based non-aqueous electrolytes for supercapacitors. Tartu, 2013, 127 p.
126. **Kerli Tõnurist.** Influence of electrospun separator materials properties on electrochemical performance of electrical double-layer capacitors. Tartu, 2013, 147 p.
127. **Kaija Põhako-Esko.** Novel organic and inorganic ionogels: preparation and characterization. Tartu, 2013, 124 p.
128. **Ivar Kruusenberg.** Electroreduction of oxygen on carbon nanomaterial-based catalysts. Tartu, 2013, 191 p.
129. **Sander Piiskop.** Kinetic effects of ultrasound in aqueous acetonitrile solutions. Tartu, 2013, 95 p.
130. **Ilona Faustova**. Regulatory role of L-type pyruvate kinase N-terminal domain. Tartu, 2013, 109 p.
131. **Kadi Tamm.** Synthesis and characterization of the micro-mesoporous anode materials and testing of the medium temperature solid oxide fuel cell single cells. Tartu, 2013, 138 p.
132. **Iva Bozhidarova Stoyanova-Slavova.** Validation of QSAR/QSPR for regulatory purposes. Tartu, 2013, 109 p.
133. **Vitali Grozovski**. Adsorption of organic molecules at single crystal electrodes studied by *in situ* STM method. Tartu, 2014, 146 p.
134. **Santa Veikšina**. Development of assay systems for characterisation of ligand binding properties to melanocortin 4 receptors. Tartu, 2014, 151 p.
135. **Jüri Liiv.** PVDF (polyvinylidene difluoride) as material for active element of twisting-ball displays. Tartu, 2014, 111 p.
136. **Kersti Vaarmets.** Electrochemical and physical characterization of pristine and activated molybdenum carbide-derived carbon electrodes for the oxygen electroreduction reaction. Tartu, 2014, 131 p.
137. **Lauri Tõntson**. Regulation of G-protein subtypes by receptors, guanine nucleotides and Mn^{2+}. Tartu, 2014, 105 p.
138. **Aiko Adamson.** Properties of amine-boranes and phosphorus analogues in the gas phase. Tartu, 2014, 78 p.
139. **Elo Kibena**. Electrochemical grafting of glassy carbon, gold, highly oriented pyrolytic graphite and chemical vapour deposition-grown graphene electrodes by diazonium reduction method. Tartu, 2014, 184 p.
140. **Teemu Näykki.** Novel Tools for Water Quality Monitoring – From Field to Laboratory. Tartu, 2014, 202 p.
141. **Karl Kaupmees.** Acidity and basicity in non-aqueous media: importance of solvent properties and purity. Tartu, 2014, 128 p.

142. **Oleg Lebedev**. Hydrazine polyanions: different strategies in the synthesis of heterocycles. Tartu, 2015, 118 p.
143. **Geven Piir.** Environmental risk assessment of chemicals using QSAR methods. Tartu, 2015, 123 p.
144. **Olga Mazina.** Development and application of the biosensor assay for measurements of cyclic adenosine monophosphate in studies of G protein-coupled receptor signalinga. Tartu, 2015, 116 p.
145. **Sandip Ashokrao Kadam.** Anion receptors: synthesis and accurate binding measurements. Tartu, 2015, 116 p.
146. **Indrek Tallo.** Synthesis and characterization of new micro-mesoporous carbide derived carbon materials for high energy and power density electrical double layer capacitors. Tartu, 2015, 148 p.
147. **Heiki Erikson.** Electrochemical reduction of oxygen on nanostructured palladium and gold catalysts. Tartu, 2015, 204 p.
148. **Erik Anderson.** *In situ* Scanning Tunnelling Microscopy studies of the interfacial structure between Bi(111) electrode and a room temperature ionic liquid. Tartu, 2015, 118 p.
149. **Girinath G. Pillai.** Computational Modelling of Diverse Chemical, Bio-chemical and Biomedical Properties. Tartu, 2015, 140 p.
150. **Piret Pikma.** Interfacial structure and adsorption of organic compounds at Cd(0001) and Sb(111) electrodes from ionic liquid and aqueous electrolytes: an *in situ* STM study. Tartu, 2015, 126 p.
151. **Ganesh babu Manoharan.** Combining chemical and genetic approaches for photoluminescence assays of protein kinases. Tartu, 2016, 126 p.
152. **Carolin Siimenson**. Electrochemical characterization of halide ion adsorption from liquid mixtures at Bi(111) and pyrolytic graphite electrode surface. Tartu, 2016, 110 p.
153. **Asko Laaniste.** Comparison and optimisation of novel mass spectrometry ionisation sources. Tartu, 2016, 156 p.
154. **Hanno Evard.** Estimating limit of detection for mass spectrometric analysis methods. Tartu, 2016, 224 p.
155. **Kadri Ligi.** Characterization and application of protein kinase-responsive organic probes with triplet-singlet energy transfer. Tartu, 2016, 122 p.
156. **Margarita Kagan.** Biosensing penicillins' residues in milk flows. Tartu, 2016, 130 p.
157. **Marie Kriisa.** Development of protein kinase-responsive photo-luminescent probes and cellular regulators of protein phosphorylation. Tartu, 2016, 106 p.
158. **Mihkel Vestli.** Ultrasonic spray pyrolysis deposited electrolyte layers for intermediate temperature solid oxide fuel cells. Tartu, 2016, 156 p.
159. **Silver Sepp**. Influence of porosity of the carbide-derived carbon on the properties of the composite electrocatalysts and characteristics of polymer electrolyte fuel cells. Tartu, 2016, 137p.
160. **Kristjan Haav**. Quantitative relative equilibrium constant measurements in supramolecular chemistry. Tartu, 2017, 158 p.

161. **Anu Teearu**. Development of MALDI-FT-ICR-MS methodology for the analysis of resinous materials. Tartu, 2017, 205 p.
162. **Taavi Ivan**. Bifunctional inhibitors and photoluminescent probes for studies on protein complexes. Tartu, 2017, 140 p.
163. **Maarja-Liisa Oldekop**. Characterization of amino acid derivatization reagents for LC-MS analysis. Tartu, 2017, 147 p.
164. **Kristel Jukk**. Electrochemical reduction of oxygen on platinum- and palladium-based nanocatalysts. Tartu, 2017, 250 p.
165. **Siim Kukk**. Kinetic aspects of interaction between dopamine transporter and *N*-substituted nortropane derivatives. Tartu, 2017, 107 p.
166. **Birgit Viira**. Design and modelling in early drug development in targeting HIV-1 reverse transcriptase and Malaria. Tartu, 2017, 172 p.
167. **Rait Kivi**. Allostery in cAMP dependent protein kinase catalytic subunit. Tartu, 2017, 115 p.
168. **Agnes Heering**. Experimental realization and applications of the unified acidity scale. Tartu, 2017, 123 p.
169. **Delia Juronen**. Biosensing system for the rapid multiplex detection of mastitis-causing pathogens in milk. Tartu, 2018, 85 p.
170. **Hedi Rahnel.** ARC-inhibitors: from reliable biochemical assays to regulators of physiology of cells. Tartu, 2018, 176 p.
171. **Anton Ruzanov.** Computational investigation of the electrical double layer at metal–aqueous solution and metal–ionic liquid interfaces. Tartu, 2018, 129 p.
172. **Katrin Kestav.** Crystal Structure-Guided Development of Bisubstrate-Analogue Inhibitors of Mitotic Protein Kinase Haspin. Tartu, 2018, 166 p.
173. **Mihkel Ilisson.** Synthesis of novel heterocyclic hydrazine derivatives and their conjugates. Tartu, 2018, 101 p.
174. **Anni Allikalt.** Development of assay systems for studying ligand binding to dopamine receptors. Tartu, 2018, 160 p.
175. **Ove Oll.** Electrical double layer structure and energy storage characteristics of ionic liquid based capacitors. Tartu, 2018, 187 p.